# A role for CASM in the repair of damaged Golgi architecture

Seeun Oh[1], Saif Ullah[1], Bhaskar Saha[3], and Michael A Mandell[1,2*]

[1] Department of Molecular Genetics and Microbiology, University of New Mexico Health Sciences Center, Albuquerque, NM 87131 USA

[2] Autophagy, Inflammation and Metabolism Center of Biomedical Research Excellence, University of New Mexico Health Sciences Center

[3] Department of Cell and Molecular Biology, Manipal School of Life Sciences, Manipal Academy of Higher Education, Manipal, Karnataka, 576104, India

* Corresponding author: mmandell@salud.unm.edu

*Running title:* TRIM46 and Golgi atg8ylation

*Keywords:* Tripartite motif, TRIM46, autophagy, CASM, VAIL, TFEB, lysosomal biogenesis, atg8ylation, microtubule, Golgi damage

*Abbreviations:* AMPK (AMP-activated protein kinase); ATG3 (autophagy related 3); ATG5 (autophagy related 5); ATG7 (autophagy related 7); ATG12 (autophagy related 12); ATG13 (autophagy related 13); ATG16L1 (autophagy related 16 like 1); BECN1 (Beclin 1); CASM, conjugation of Atg8 to single membranes; GABARAP (GABA type A receptor-associate protein); GABARAP L1 (GABA type A receptor-associate protein like 1); GABARAP L2 (GABA type A receptor-associate protein like 2); HT (HaloTag); HL (HaloTag ligand); hVPS34/PIK3C3 (phosphatidylinositol 3-kinase catalytic subunit type 3); LC3A (microtubule associated protein 1 light chain 3 alpha); LC3B (microtubule associated protein 1 light chain 3 beta); LC3C (microtubule associated protein 1 light chain 3 gamma); mTORC1 (mechanistic target of rapamycin complex 1); PE (phosphatidyl ethanolamine); PS (phosphatidyl serine); TECPR1 (tectonin beta-propellor repeat containing 1); TFEB (transcription factor EB); TFE3 (transcription factor binding to IGHM enhancer 3); TGN46/TGOLN2 (trans-golgi network protein 2); TRIM46 (tripartite motif containing 46); ULK1 (unc-51 like autophagy activating kinase 1); VAIL (V-ATPase-ATG16L1induced LC3 lipidation)

**ABSTRACT**

The term CASM describes a process in which LC3 and other Atg8 proteins are covalently ligated to lipids in damaged endomembranes. While CASM is commonly described as a cytoprotective response to multiple types of membrane damage, the ways in which CASM helps cells maintain homeostasis are still unclear. Here, we show that CASM contributes to the maintenance or repair of Golgi apparatus architecture following the loss of TRIM46, a ubiquitin ligase with roles in microtubule organization. TRIM46-deficient cells were notable for enhanced TFEB-driven lysosomal biogenesis and Golgi ribbon fragmentation, with colocalization between the *trans*-Golgi marker TGN46 and the Atg8 proteins LC3B and GABARAP. Similar results were seen when Golgi architecture was disrupted by inhibitors of microtubule assembly or of vesicle trafficking. Further studies revealed that the Golgi atg8ylation seen in TRIM46 knockout cells was not degradative and mechanistically resembled CASM. Genetic inhibition of CASM in TRIM46-deficent cells reduced TFEB activation and exacerbated the Golgi morphology defects. Together, these studies reveal that lysosomal biogenesis and CASM are common features of a Golgi damage response, with CASM acting to preserve Golgi integrity.

## INTRODUCTION

The proper organization, placement, and maintenance of membranous organelles is fundamental to the life of eukaryotic cells. This requires the repair or replacement of damaged membranes or dysfunctional membrane-associated proteins. Multiple mechanisms of membrane repair have evolved, likely due to the critical importance of maintaining membrane integrity and function, the diversity of organelle membranes within a cell, and the variety of possible causes of membrane damage. Depending on the type of membrane damage, cellular responses can include: i) ESCRT-mediated excision of damaged membranes; ii) delivery of new membrane to the site of damage by organelle fusion or by membrane-to-membrane lipid transfer; and iii) enhanced expression and biosynthesis of protein constituents of damaged membranes[1]. Additionally, multiple membrane damage scenarios trigger the attachment of a set of ubiquitin-like proteins, collectively referred to as Atg8s (LC3A, LC3B, LC3C, GABARAP, GABARAP L1, and GABARAP L2), to membrane in a process termed 'atg8ylation'[2-4].

Membrane atg8ylation contributes to membrane damage responses in several ways. These include enabling the lysosome-mediated removal of damaged membranes or membranous organelles[5-8], indirectly up-regulating the biosynthesis of new membrane components[9-11], and providing a "patch" to plug damaged membranes[12]. Mechanistically, the atg8ylation process resembles ubiquitylation, with the roles of E1 activating enzyme and E2 conjugating enzyme played by ATG7 and ATG3, respectively[3]. There are two multi-protein E3 ligase complexes that are known to act in atg8ylation: the ATG5-ATG12-ATG16L1 complex[13] and the ATG5-ATG12-TECPR1 complex[14,15]. The E3 ligase complexes attach Atg8 proteins to either phosphatidylethanolamine (PE) or phosphatidylserine (PS). Macroautophagy (hereafter, autophagy) is the best-studied pathway that utilizes membrane atg8ylation. In autophagy, Atg8 proteins are attached to *de novo*-created membrane that elongates in a curved manner and ultimately sequesters cytoplasmic contents within a sealed double-membraned vesicle termed an autophagosome[16]. Autophagosomes are then trafficked along microtubules towards lysosomes, where the two organelles fuse and the inner autophagosomal membrane and its luminal contents are degraded[17]. More recently, additional processes that require the atg8ylation machinery have been identified. These processes differ from autophagy in that they involve atg8ylation of pre-existing membranes, they do not result in the formation of autophagosomes, and they are not always degradative[2]. The term CASM (conjugation of Atg8 to single membranes) has been coined to describe these atg8ylation-dependent pathways[18]. While both autophagy and CASM utilize the same atg8ylation machinery, they differ in the

mechanism by which the E3 ligase complex is recruited to the sites of atg8ylation. In autophagy, the ATG16L1-containing E3 complex is recruited to phosphatidylinositol-3-phosphate containing membranes generated by the BECN1/hVPS34 complex. The BECN1 (Beclin 1) complex is activated by a protein complex containing the kinase ULK1/2. On the other hand, BECN1 and the ULK1 complex are dispensable for CASM[18-20]. Finally, the two pathways differ in terms of which lipid is conjugated to Atg8s, with PE being exclusively utilized by autophagy whereas both PE and PS are utilized by CASM[21]. Despite their mechanistic differences, both autophagy and CASM are typically considered protective responses to membrane damage, although the functions of CASM remain largely undefined.

Ubiquitination can be a key regulator of atg8ylation-dependent processes[22]. This is particularly true in the case of autophagy. For example, many members of the tripartite motif containing (TRIM) family of ubiquitin ligases are reported to act as both autophagy regulators and in the identification of membranous or proteinaceous autophagy substrates[23-25]. The role(s) of TRIM proteins, or ubiquitination more generally, in other atg8ylation-dependent processes such as CASM have not yet been explored.

Here, our investigation into the actions of TRIM proteins in atg8ylation led us to find that disruption of microtubule organization is a potent activator of the non-degradative atg8ylation of *trans*-Golgi membranes. This subsequently activates a program of lysosomal biogenesis and autophagy activation. We found that TRIM46, a ubiquitin ligase previously implicated in the formation of an axonal structure in neurons[26], is important for microtubule organization. Genetic depletion of TRIM46 resulted in fragmentation of the *trans*-Golgi network (TGN) and activated TFEB/TFE3, the master transcriptional activators of lysosome- and autophagy-related gene expression. TRIM46 knockout also resulted in substantial atg8ylation of the TGN in a manner reminiscent of CASM. When atg8ylation is blocked, the Golgi morphology defects seen in TRIM46 knockout cells were exacerbated, while the activation of TFEB was attenuated. The activation of both CASM and TFEB seen in TRIM46 knockout is phenocopied by chemical inhibitors of microtubule function or vesicle trafficking, all of which disrupt Golgi architecture. Overall, our study indicates that CASM-dependent activation of lysosomal biogenesis is a general response perturbations of Golgi architecture, with CASM having a role in membrane repair or reorganization.

## RESULTS

### Screening of TRIM proteins for roles in autophagosome maturation.

Since TRIM proteins have many reported roles in regulating autophagy initiation[23,27,28], we wondered if their actions in autophagy extend to mediating autophagosome-lysosome fusion and autophagy flux. To address this question, we reanalyzed data from a previous siRNA screen that examined the effect of TRIM knockdown on the abundance of the autophagosome marker LC3B[29]. This screen made use of cells expressing mCherry-eYFP-LC3B (tandem fluorescent LC3B, tfLC3B) as a marker of autophagosomes. Although tfLC3B can be used to monitor both the formation of autophagosomes and their delivery to lysosomes (termed autophagosome maturation) due to the differential sensitivity of the two fluorophores to low pH[30,31], in our initial analysis we only considered the abundance of YFP-positive LC3B structures[29]. Here, we determined whether the siRNA-mediated knockdown of any one of 68 TRIMs in HeLa cells altered the delivery of the LC3B reporter to acidified compartments, which can be detected by comparing the relative abundance of “non-acidified” LC3B structures (positive eYFP signal) with that of “total” LC3B structures (positive for mCherry signal; Fig. 1A, B and S1A). We found that cells subjected to knockdown of six TRIMs (TRIMs 25, 38, 46, 47, 61, and 68) reduced the acidification of the LC3B reporter by more than three standard deviations below the mean of cells transfected with non-targeting siRNAs in two out of two experiments (Fig. 1B and S1A). This indicates a possible role for these TRIMs in autophagosome maturation. Alternatively, these TRIMs could act to inhibit non-degradative atg8ylation pathways such as CASM.

### Knockdown of TRIM46 increases non-degradative atg8ylation without impairing autophagy flux.

We chose to focus on TRIM46 as a possible regulator of autophagosome maturation because of its reported actions on microtubule organization in neurons, which we reasoned could impact proper autophagosome and/or lysosome trafficking. We generated several clonal populations of HeLa and HEK293T cells in which TRIM46 was knocked out by CRISPR/Cas9 (Fig. S1B, C). High content imaging of two of the HeLa cell lines showed that the abundance of endogenous LC3B puncta was elevated by ~3-fold in the TRIM46 knockout cells relative to wild-type HeLa cells stably expressing Cas9 and non-targeting gRNA (Fig. 1C, D). Immunoblot experiments also showed that TRIM46 knockout HeLa cells (Fig. 1E, F) or HEK293T cells (Fig. S1D) showed strongly elevated levels of LC3B-II, the form of LC3B that is generated by atg8ylation. Exogenous expression of TRIM46 reversed the effect of TRIM46 knockout on LC3-II abundance

(Fig. S1E, F). Together, these data show that TRIM46 attenuates the accumulation of lipidated LC3B.

Although the purpose of our initial screen was to identify TRIMs that might be required for autophagosome maturation, further study showed that TRIM46 deficiency did not impair autophagy flux. This was first demonstrated using the Halo-LC3 assay, which relies on the fact that Halo tag/Halo ligand adducts (HT/HL) are protected from lysosomal degradation. When autophagy flux is active, the lysosome will incompletely degrade HT/HL-fused LC3 (48 kDa), leaving a 33 kDa HT/HL fragment that can readily be detected in SDS-PAGE gels when the Halo ligand is fused to a fluorescent molecule[32]. We detected the HT/HL fragment in lysates from both WT and TRIM46 knockout cells expressing HT-LC3B and treated with tetramethylrhodamine (TMR)-labeled HL under basal autophagy conditions (Fig. 1G). Although more released HT/HL is present in TRIM46 knockout cells, quantitation of the released HT/HL band relative to the total abundance of TMR signal (Fig. 1H) indicated that WT and TRIM46 knockout cells had comparable levels of autophagy flux. Image analysis showed that colocalization between LC3B and the lysosome marker LAMP2 in both lines of TRIM46 knockout HeLa cells was elevated relative to WT (Fig. 1I, J and S1G, H), indicating no impairment in autophagosome/lysosome fusion. Treatment with the lysosomal inhibitor Bafilomycin A1 (BafA1) increased the abundance of the autophagy substrate SQSTM1 in both WT and TRIM46 knockout cells (Fig. 1K, L), demonstrating functional autophagy flux.

Interestingly, however, the effect of BafA1 on LC3-II levels in TRIM46 knockout cells was muted relative to what was measured in WT cells in which it strongly increased the abundance of LC3-II (Fig. 1K, M). Similar results were seen when using the Halo-LC3 assay (Fig. S1I). BafA1 treatment increased the abundance of HT/HL-LC3B-II in WT cells pulsed with TMR-HL by ~3-fold. In contrast, BafA1 had no effect on the abundance of HT/HL-LC3B-II in the TRIM46 knockout cells. As discussed later, our interpretation for this result as well as those from our tfLC3B experiments (Fig. 1B and S1A) is that not all of the membrane-associated LC3B in TRIM46 knockout cells is delivered to acidified compartments for degradation and that atg8ylation pathways in addition to autophagy are activated in TRIM46-deficient cells.

**TRIM46 restrains lysosomal biogenesis**

In the experiments shown in Figure 1I and S1E, we noted that the number of LAMP2-positive structures appeared elevated in the TRIM46 knockout cells, a result that we confirmed by high content imaging (Fig. 2A, B). The expression of membrane and luminal proteins of lysosomal proteins also tended to be higher in TRIM46 knockout HeLa cells (Fig. 2C, D) and HEK293T

cells (Fig. S2A, B). Thus, lysosomal abundance is increased in TRIM46 knockout cells. To further assess lysosomal function in TRIM46 knockout cells, we used DQ-BSA, a molecule that becomes fluorescent upon hydrolysis by lysosomal proteases in an acidic environment[33]. TRIM46-knockout cells exhibited increased DQ-BSA signal relative to WT cells (Fig. S2C, D). However, when DQ-BSA signal was normalized to the abundance of lysosomes based on LAMP2 staining, TRIM46 knockout cells were indistinguishable from WT (Fig. S2E). This indicates that the degradative functions of lysosomes are intact in TRIM46 knockout cells. These data suggest that the increased lysosome abundance is not due to the accumulation of dysfunctional lysosomes, but instead due to lysosomal biogenesis.

Lysosomal biogenesis is controlled at the transcriptional level by the MiTF/TFE family of transcription factors, which includes the protein TFEB. TFEB shuttles between the cytoplasm and nucleus depending on its phosphorylation status to activate the expression of a large number of autophagy- or lysosome-related genes[34-36]. TFEB staining revealed that TRIM46-knockout cells exhibited a nearly two-fold increase in TFEB nuclear localization compared to WT cells (Figure 2E, F), consistent with enhanced lysosomal biogenesis in TRIM46 knockout cells. TFEB is under the control of the master metabolic regulating kinases mTORC1 and AMPK[36-40]. TRIM46 knockout reproducibly increased the level of active phosphorylated AMPK while the phosphorylation of p70 S6 kinase, a substrate of mTORC1, was decreased (Fig. 2G-I). Active mTORC1 is primarily localized on lysosomes[41]. In confocal microscopy experiments, we found that the lysosomal localization of mTOR was reduced in TRIM46 knockout cells (Fig. S2F, G), further indicating reduced mTORC1 activation. Overall, these data show that TRIM46 restrains TFEB-mediated lysosomal biogenesis associated with mTORC1 inactivation.

**_trans_-Golgi apparatus is disrupted and subject to non-degradative atg8ylation in TRIM46 knockout cells.**

We next considered how TRIM46 deficiency triggered TFEB activation. As the master regulator of lysosome biogenesis, TFEB activation is strongly associated with lysosomal damage[42,43]. However, our data shown in Fig. S2 indicates that the lysosomes in TRIM46 knockout cells are functional. We thus considered whether damage to other organelles could explain the phenotypes observed in TRIM46 knockout cells. Structural disruption of the Golgi has been reported to inactivate mTOR signaling while inducing atg8ylation[9,44,45]. The architecture of the Golgi apparatus is maintained by microtubules[46,47]. TRIM46 localizes to microtubules and has been implicated in bundling axonal microtubules in neurons[26]. We thus hypothesized that Golgi structure might be disrupted in TRIM46 knockout cells via microtubule disorganization, and that

this may explain the mTOR and TFEB phenotypes that we have observed. In agreement with this hypothesis, we found that mCherry-tagged TRIM46 exclusively localized to microtubules when expressed in HeLa cells (Fig. S3A). The microtubules in TRIM46 knockout cells were shorter and more disorganized than in WT cells (Fig. 3A-C). Along with the microtubule phenotypes, we observed that the Golgi apparatus in TRIM46 knockout cells appeared to be larger and less coalesced. We also noticed that the number of small structures positive for the trans-Golgi marker TGOLN2/TGN46 (trans-Golgi network protein 2; TGN46) was substantially increased in TRIM46 knockout cells (Fig. 3D). As a measure of Golgi fragmentation, we used high content imaging and analysis to selectively identify “small” TGN46-positive structures (smaller than 3 $\mu m^2$) and quantitate them in WT and TRIM46 knockout cells. Using this analysis, we saw that the number of Golgi fragments was increased by ~2-fold in both TRIM46 knockout cell lines relative to WT (Fig. 3E and S3B). Additionally, the total area of TGN46, including both small and large TGN46-positive structures, is increased in TRIM46 knockout cells (Fig. 3F). Although imaging analysis revealed an increased Golgi area in TRIM46 knockout cells, the abundance of Golgi-resident proteins including GCP60 and the *trans*-Golgi protein TGN46 was unchanged, and only a slight increase was observed in the endosomal/TGN localized protein WIPI1 (Fig. S3C). These findings suggest that the increased Golgi area reflects structural dispersal rather than an upregulation of Golgi protein synthesis in TRIM46 knockout cells. Together, these data demonstrate that TRIM46 is essential for maintaining Golgi architecture, likely through TRIM46’s ability to organize microtubules.

In our siRNA screen (Fig. 1), we observed that TRIM46 knockdown increased the abundance of non-acidified LC3B structures, suggesting that TRIM46 may inhibit a non-degradative atg8ylation pathway. Several other groups have observed non-degradative conjugation of LC3 to Golgi membranes[9,45,48], and so we wondered if some of the LC3-positive structures seen in TRIM46 knockout cells colocalized with the *trans*-Golgi marker TGN46. Indeed, we found substantial overlap between the small TGN46-positive structures and the Atg8 proteins LC3B and GABARAP in TRIM46 knockout cells (Fig. 4A-F; S4A-B). Analysis of three-dimensional reconstructions of deconvolved confocal images of TRIM46 knockout cells that had been probed with antibodies recognizing TGN46 and LC3B revealed that the LC3B-positive structures that colocalized with TGN46 had irregular morphologies that corresponded with the shape of the TGN46 structure (Fig. S4C). The shape of these LC3B-positive structures was different from what might be expected of autophagosomes, which tend to be round. In agreement with this observation, quantitative analysis showed that the LC3B-positive structures in TRIM46 knockout cells showed reduced sphericity when compared to LC3B-positive structures in WT cells (Fig.

S4D). Subcellular fractionation experiments also indicated association between lipidated LC3B and TGN46-positive membranes (Fig. S4E). To enrich lysosomal and trans-Golgi network (TGN) vesicles, we performed sequential, differential centrifugation including ultracentrifugation at 100, 000 g. The resulting pellets were lysed, and equal amounts of protein were analyzed. Fractionation was confirmed by immunoblotting with LAMP2 and TGN46 as lysosomal and TGN markers, respectively. In WT cells, lipidated LC3B was predominantly found in 21k fraction, with substantially less LC3B-II cofractionating with TGN46 in the 100k fraction. In contrast, roughly equal amounts of LC3B-II were found in the 21k and 100k fractions in TRIM46 knockout cells (Fig. S4E). The findings presented above are consistent with direct conjugation of LC3B to the TGN46-positive membranes. In agreement with this concept, ATG16L1, a key component of the atg8ylation machinery, shows strongly enhanced colocalization with TGN46 in TRIM46 knockout cells (Fig. 4G and S4F-H). We next used mKeima-fused YIPF3 as a reporter to determine if the atg8ylated Golgi fragments were delivered to the lysosome for degradation in a selective autophagy-based process called 'Golgiphagy'[7,49,50]. YIPF3 is a Golgi-resident transmembrane protein that serves as a Golgiphagy receptor and is degraded by autophagy following amino acid starvation[49,50]. We saw no difference in the delivery of the mKeima-YIPF3 reporter to acidified compartments when we compared WT with TRIM46 knockout cells, despite positive controls (amino acid starvation) and negative controls (BafA1) behaving as expected in this assay (Fig. S4I). These results, along with data showing that TRIM46 knockout does not reduce the abundance of several Golgi-resident proteins (Fig. S3C), show that TRIM46 knockout does not increase Golgiphagy, and instead imply that the observed Golgi atg8ylation is non-degradative.

**TRIM46 knockout activates CASM of *trans*-Golgi membranes**

Our data indicate that TRIM46 knockout induces CASM-mediated atg8ylation of TGN46-positive membranes. To further validate this, we inhibited or knocked down proteins that are essential for autophagy but are dispensable for CASM[51-53]. When WT cells are treated with VPS34-IN1, a compound that inhibits phagophore formation, LC3-II levels were reduced by ~60%. In contrast, this treatment only modestly impacted LC3B-II levels in TRIM46 knockout cells (~20% reduction; Fig. 5A, B). Next, we employed siRNA to knock down the expression of the core autophagy proteins ATG7, ATG13, BECN1, and ULK1 to determine how this impacted the elevated levels of LC3-II and the increased abundance of LC3-positive structures in TRIM46 knockout cells (Fig. 5C-F; S5A-F). As expected, knockdown of ATG7 reduced lipidated LC3B and LC3B puncta. ATG7 knockdown also reduced the colocalization between LC3B and TGN46

(Fig. 5G; S5C). However, knocking down the expression of ATG13 and BECN1 did not reduce the abundance of LC3-II or LC3 puncta in TRIM46 knockout cells. ULK1 knockdown seemed to reduce atg8ylation in TRIM46 knockout cells, but this trend was not statistically significant (Fig. 5C-G; S5D-G). These data confirm that much of the excessive atg8ylation seen in TRIM46 knockout cells is attributable to CASM.

Deacidification of cellular compartments such as lysosomes or ER is a known driver of CASM[54]. This process, also called VAIL (V-ATPase-ATG16L1-induced LC3 lipidation)[55], requires the complete assembly and activity of V-ATPase structures on the membranes of the deacidified organelles[56]. V-ATPase then recruits the ATG16L1 E3 ligase complex through direct protein-protein interaction[57]. We asked whether V-ATPase assembly is required for the elevated atg8ylation seen in TRIM46-knockout cells. V-ATPase-dependent LC3 lipidation can be blocked by BafA1[55], which inhibits V-ATPase assembly. However, the inhibitory effects of BafA1 on CASM-related atg8ylation can be hard to detect since BafA1 also causes the accumulation of autophagy-related lipidated LC3B. To overcome this challenge, we used VPS34-IN1, which minimally impacts atg8ylation in TRIM46 knockout cells (Fig. 5A, B) to block autophagy while simultaneously treating cells with BafA1. When this experiment was performed on WT cells, our results indicated that autophagy was the primary driver of atg8ylation, with BafA1 treatment increasing and VPS34IN-1 decreasing the abundance of LC3B-II. VPS34-IN1 completely prevented the BafA1-dependent accumulation of lipidated LC3B (Fig. 5H). In contrast, TRIM46 knockout cells showed evidence for both ongoing autophagy and CASM, since neither BafA1 nor VPS34IN-1 on their own impacted the already elevated levels of lipidated LC3B seen in these cells. However, the levels of LC3B-II were significantly reduced when TRIM46 knockout cells were treated with both inhibitors (Fig. 5H). Thus, when autophagy is inhibited with VPS34-IN1, we can see a clear inhibitory effect of BafA1 on atg8ylation in TRIM46-deficient cells. This result establishes a role for the V-ATPase in Golgi membrane atg8ylation in TRIM46-deficient cells.

**Impacts of CASM on TFEB activation and Golgi morphology in TRIM46-deficient cells**

In most cases, the physiological consequences of CASM are not entirely clear. We next used ATG7 knockdown to determine whether atg8ylation contributes to the phenotypes seen in TRIM46 knockout cells. We found that siRNA-mediated knockdown of ATG7 expression substantially reduced the percentage of TRIM46 knockout cells that were positive for TFEB nuclear localization (Fig. 5I), suggesting that CASM may contribute to the increased lysosomal biogenesis seen in TRIM46 knockout cells. Our data also indicate a role for CASM in governing

Golgi architecture in TRIM46 knockout cells. As discussed above, the trans-Golgi network in TRIM46 knockout cells is disrupted and shows an increased area per cell (Fig. 3D-F). We found that ATG7 knockdown in TRIM46 knockout cells exacerbated this phenotype, further increasing the cross-sectional area of TGN46 staining per cell relative to TRIM46 knockout cells transfected with non-targeting siRNA (Fig. 5J). Since we did not see evidence of Golgiphagy (Fig. S3C and S4I), we assume that Golgi atg8ylation is likely serving to either maintain or repair Golgi architecture.

**Chemical disruption of the Golgi architecture phenocopies TRIM46 knockout**

We have demonstrated that TRIM46 deficiency leads to disorganization of the microtubule network, Golgi fragmentation, and CASM activation. To determine whether microtubule disorganization alone is sufficient to mimic the phenotypes seen in TRIM46 knockout cells, we treated WT HeLa cells with the microtubule-depolymerizing agents vinblastine and nocodazole. As expected, both treatments significantly increase TGN46-positive fragments (Fig. 6A, B and S6A, B). Similar to TRIM46 knockout cells, both vinblastine- and nocodazole-treated cells showed a significant increase in LC3B puncta and LC3B/TGN46 colocalization, suggesting CASM activation (Fig. 6C-F; S6C-E). Microtubule disruption also increased lysosome abundance (Fig. 6G, H; S6F-G) and increased TFEB nuclear localization (Fig 6I, J; S6H-I), mirroring the effects observed in TRIM46 knockout cells. Thus, disorganization of the microtubule network, whether by drug treatment or by TRIM46 deficiency, results in CASM and lysosomal biogenesis.

We next asked whether we could recapitulate the phenotypes seen in TRIM46 knockout cells by disrupting Golgi apparatus architecture without targeting microtubules. To test this, we treated HeLa cells with brefeldin A, a compound that induces Golgi disassembly by interfering with the formation of COP-I vesicles. As expected, brefeldin A increased the number of Golgi fragments per cell in WT HeLa cells (Fig. S6J, K). Additionally, we found that it also significantly increased the abundance of LC3B puncta per cell and the colocalization between LC3B and TGN46 (Fig. S6L-N). Brefeldin A treatment also resulted in a >2-fold increase in TFEB nuclear localization (Fig. S6O, P). These data show that Golgi atg8ylation and TFEB activation are generalized cellular responses to disruption of Golgi architecture.

## DISCUSSION

Golgi architecture disruption is associated with multiple pathological conditions including viral infection, cancer, and neurodegenerative disease[58-62]. How cells respond to or repair these architectural changes remains unclear. Our study has shown that disruption of the Golgi apparatus activates a generalized response including Golgi atg8ylation and TFEB-driven lysosomal biogenesis (Fig. 6K). We started our studies focusing on TRIM46, which likely alters Golgi structure indirectly through its actions in establishing microtubule organization. Supporting this concept, we found that treatment of wild type cells with the microtubule depolarizing compounds vinblastine or nocodazole phenocopied what we observed with the TRIM46 knockout cells. Interestingly, brefeldin A, which disrupts Golgi structure and function without impacting microtubule organization, also induced Golgi atg8ylation and TFEB activation. This result suggests that loss of Golgi architecture, rather than disruption of microtubule organization, is the primary trigger for these phenotypes. In agreement with this concept, blockage of post-Golgi trafficking by over-expression of the secreted protein DLK1[9], down-regulation of a Golgi-localized membrane tether[63], or various Golgi-damaging treatments[45,64] all induce LC3 conversion.

Key questions remain about why cells engage the atg8ylation machinery in response to Golgi or other membrane stress. We found that TRIM46 deficiency constitutively activated Golgi atg8ylation. Inhibition of Golgi atg8ylation by knocking down ATG7, the E1 activating enzyme of the atg8ylation cascade, had two effects in TRIM46 knockout cells. First, it augmented the Golgi architecture defects caused by TRIM46-deficiency. This suggests that atg8ylation plays a role in the maintenance or repair of the Golgi ribbon structure, since our data excluded the possibility that Golgiphagy was responsible for removing damaged Golgi fragments in TRIM46 knockout cells. Our data also disfavors models in which atg8ylation results in increased Golgi biosynthesis or the delivery of new membrane to damaged Golgi structures, since these mechanisms would be expected to add size to the Golgi in an ATG7-dependent manner, which is the opposite of what we found. Further investigation is needed to identify how atg8ylation acts to control Golgi architecture.

Second, we found that the increased activation of the transcription factor TFEB seen in TRIM46 knockout cells was reversed following ATG7 knockdown. This result is consistent with several other recent findings that revealed a positive feedback loop between atg8ylation and TFEB activation[10,11]. Golgi damage, by either TRIM46 deficiency or by chemical disruption of the Golgi network, strongly promotes TFEB activation to enhance lysosomal biogenesis and upregulate

the expression of proteins involved in CASM and autophagy. We speculate that the TFEB-dependent responses to Golgi damage may be a cellular response to counter the source of Golgi damage or possibly in preparation to initiate Golgiphagy should the extent of Golgi damage become more severe. The second concept aligns with what is known about lysosomal membrane permeabilization, in which CASM is activated in response to mild lysosomal damage while lysophagy, the autophagic targeting of damaged lysosomes, seems to be reserved for lysosomes that are extensively damaged[65]. It is possible that a similar relationship exists with Golgi membranes: while TRIM46 knockout does not cause sufficient damage to induce Golgiphagy, complete disruption of Golgi architecture with Brefeldin A is reported to induce autophagic degradation of Golgi-localized proteins[64].

Our studies with TRIM46, as well as other observations of Golgi atg8ylation in response to a variety of Golgi damaging conditions, raise the question of how the cell senses Golgi damage to activate atg8ylation. However, it is currently unknown if all of the various causes of Golgi damage activate the same damage-sensing pathways or if different forms of Golgi damage trigger different danger signals. Since the Golgi is a slightly acidic organelle, it is possible that some of the aforementioned Golgi damaging conditions could lead to proton leak and consequent deacidification of the Golgi lumen. In membranes of the endolysosomal system, this will lead to CASM in a manner requiring assembly of active V-ATPase complexes which recruits ATG16L1 complexes[54]. Our data demonstrating that TRIM46 knockout increases ATG16L1 recruitment to Golgi membranes and that V-ATPase inhibition with BafA1 reduces LC3 lipidation in TRIM46 knockout cells are consistent with this model. Lysosomal deacidification also results in mTORC1 inactivation[41]. Interestingly, several studies have indicated that a pool of mTORC1 resides on the Golgi in addition to its well-established localization on lysosomes[63,66,67]. We found that mTORC1 activity was inhibited in TRIM46-deficient cells, suggesting similar damage-responsive mechanisms between Golgi and lysosomes. Inhibition of mTORC1 activity can then result in or enhance autophagy and lysosomal biogenesis while also altering Golgi architecture[67,68].

Given the broad functions of TRIMs in autophagy, our initial goal was to screen TRIMs for roles in the late stages of autophagy. Interestingly, follow up experiments demonstrated that TRIM46 deficiency led to non-degradative CASM activation. In addition to TRIM46, the knockdown of five other TRIMs also showed reduced LC3B acidification in our screen (Fig. 1). Further investigations are warranted to determine whether these TRIMs regulate atg8ylation pathways indirectly, as in the case with TRIM46, or if they directly regulate autophagosome maturation.

In conclusion, our study shows that TRIM46 contributes to the organization of the microtubule network. TRIM46 deficiency destabilized microtubules and resulted in alteration to the Golgi ribbon structure, triggering CASM, lysosomal biogenesis, and changes in the activity of the key metabolic regulators mTORC1 and AMPK. Our work extends the growing body of literature documenting Golgi atg8ylation by demonstrating that CASM functions to maintain or repair Golgi architecture in response to Golgi damage.

**Acknowledgements**

This work was supported by R01AI155746 to M.A.M from the US National Institutes of Health. S.O. was supported by T32AI007538 from the National Institute of Allergy and Infectious Disease. Confocal microscopy and flow cytometry were performed in the University of New Mexico Comprehensive Center shared resources, which are partially supported by P30CA118100 form the NIH. High content imaging was performed in the Autophagy, Inflammation, and Metabolism (AIM) Center core facility, which is supported by P20GM121176 from the NIH. Dr. Ruheena Javed (University of New Mexico) provided technical advice, and Drs. Thabata Duque, Tae-Hyung Kim, and Joseph Endicott (University of New Mexico) commented on the manuscript. Biorender software was used to generate graphics.

**Author contributions**

S.O., S.U., B.S., and M.A.M performed research. S.O. and M.A.M. analyzed data and wrote the paper. The authors declare that they have no conflict of interest.

## METHODS

### Antibodies

Primary antibodies were obtained as follows: mCherry (ab183628), GABARAP (ab109364; 1:500 for IF), and NPC2 (ab2181921:1,000 for WB) from Abcam; AMPK (2532; 1:1000 for WB), phospho-AMPK T172 (2535; 1:1,000 for WB), ATG13 (13468; 1:1,000 for WB), BECN1 (3459; 1:1,000 for WB), GM130 (12480; 1:500 for IF, 1:1,000 for WB), mTOR (2983; 1:500 for IF), phospho-P70 S6K (9205; 1:1,000 for WB), TFEB (4240; 1:500 for IF), and ULK1 (8054; 1:1,000 for WB) from Cell Signaling Technology; actin (sc-58673; 1:1,000 for WB), Cas9 (sc-517386, 1:1000 for WB), LAMP2 (sc-18822; 1:1,000 for WB, 1:500 for IF), P70 S6K (sc-8418; 1:1,000 for WB), and alpha-tubulin (sc-23948; 1:500 for IF) from Santa Cruz Biotechnology; Cathepsin D (21327-1-AP, 1:1,000 for WB), myc (16286-1-AP: 1:1,000 for WB), LIMP2 (27102-1-AP, 1:1,000 for WB), TRIM46(21026-1-AP, 1:1,000 for WB) from Proteintech; LC3B (PM036; 1:500 for IF) from MBL and LC3B (L7543; 1:2,000 for WB) from Sigma; p62/SQSTM1(610833 ; 1:2,000 for WB) from BD; ATG7 (MA5-32221; 1:1,000 for WB), GCP60 (MA5-25999; 1:1,000 for WB), TGN46 (MA5-37930; 1:1,000 for WB), and WIPI1 (PA5-34973; 1:1000 for WB) from Thermo Fisher and TGN46 (AHP500G; 1:500 for IF) from Bio-Rad. Secondary antibodies were purchased as follows: anti-rabbit Alexa Fluor 488 (A11008; 1:1,000 for IF), anti-sheep Alexa Fluor 568 (A21099; 1:1,000 for IF), anti-rabbit Alexa Fluor 647 (A21244; 1:1,000 for IF), and anti-mouse Alexa Fluor 647 (A21235; 1:1,000 for IF) from Thermo Fisher; anti-mouse IRDye 680LT (925-68020; 1:10,000 for WB) and anti-rabbit IRDye 800CW (926-32211; 1:5,000 for WB) from LI-COR.

### Cell culture and treatment

All cell lines were maintained in Dulbecco's modified Eagle's medium (DMEM; 11965084, Thermo Fisher) supplemented with 10% fetal bovine serum (FBS; 26140095, Thermo Fisher) and 100 U/mL penicillin-streptomycin (15140122, Thermo Fisher) in a humidified incubator at 37 °C with 5% $CO_2$. Bafilomycin A1 (tlrl-baf1, Invivogen; 100 μM), brefeldin A (B6542, Sigma; 5 mM), nocodazole (M1404, Sigma; 5 mM), Vps34-IN1 (Cayman chemical; 10 mM), vinblastine (11762, Cayman chemical; 100 μM) were prepared as stock solution in DMSO at the indicated stock concentration. To measure autophagy flux and CASM in TRIM46 knockout cells, cells were treated with 100 nM bafilomycin A1 with or without 10 μM vps34-IN1 for 4 or 6 hours. For

experiments examining TFEB nuclear localization or LC3B and LAMP2 induction, cells were treated with 100 nM brefeldin A, nocodazole, or vinblastine for 16 hours.

**Development of knockout or overexpressing cell lines**

Knockout and stably overexpressing cell lines were generated by lentiviral transduction. Lentivirus was produced by co-transfecting HEK293T cells with pMD2.G, pPAX2, and pLV[CRISPR]-hCas9:T2A:Puro-U6-hTRIM46 (VB900138-6978huh, VectorBuilder) or pLEX307-Halo-LC3 at a 2:3:5 ratio using the ProFection Mammalian Transfection System (Promega). After 48hours, virus-containing supernatants were collected, cleared of residual mammalian cells by centrifugation at 500 × g for 10 minutes, and filter through a 0.45 μm vacuum filter (SE1M003M00, SIGMA). Target cells (HeLa or HEK293T) were incubated with viral supernatants diluted in DMEM for 48 hours and subsequently selected with 1 μg/mL puromycin (J61278.MB, Thermo Fisher). For TRIM46 knockout cells, single-cell clones were isolated, and knockout was validated using the Guide-it Complete sgRNA Screening System (632636, Takara). Briefly, sgRNA targeting TRIM46 was generated using a customized forward PCR primer containing T7 promoter sequence, TRIM46 target sequence, and Cas9 scaffold templates with the Guide-it sgRNA *In Vitro* Transcription Kit (Takara). The sgRNA template was validated on a 2% agarose gel, which showed a single band of ~130 bp. sgRNA was synthesized by *In Vitro* transcription using the validated template. Genomic DNA was extracted from WT or TRIM46 knockout cells using a genomic DNA extraction kit (95213-050, QuantaBio), and the target region containing the CRISPR/Cas9 cleavage site was amplified by PCR. After purification of PCR fragments, the Cas9 cleavage assay was performed. The reaction products were loaded on a 1.5% agarose gel and imaged using a ChemiDoc Imaging System (Bio-Rad). For Halo-LC3B expressing HeLa wild type or TRIM46 knockout cells, Halo-LC3B expression was confirmed by immunoblotting with anti-HaloTag antibody.

**RNA interference and transfection**

Plasmid transfections were performed using Lipofectamine 2000 (ThermoFisher). Small interfering RNAs (siRNAs) were purchased from GE Dharmacon and were supplied as pools of four different siRNA oligos against the same mRNA. siRNA transfections were performed using Lipofectamine RNAiMAX (ThermoFisher) according to the manufacturer’s instructions.

## Cloning

pDONR221-hTRIM46 (HsCD00862242, DNASU) was used as the donor for cloning human TRIM46 into Gateway-compatible destination vectors, generating myc- or mCherry-tagged TRIM46 using LR Clonase (11791020, Thermo Fisher). All Plasmid constructs were verified by whole-plasmid sequencing. For addback experiments, the PAM site in myc- or mCherry-tagged TRIM46 was disrupted to prevent degradation by constitutively expressing Cas9 in TRIM46 knockout cells by introducing a silent mutation (1407G→T) using a site-directed mutagenesis kit (210518, Agilent).

## TRIM family siRNA screen

The methods employed for this experiment, and the results from analyzing eYFP signal on its own, were previously published[29]. Briefly, HeLa cells expressing mCherry-eYFP-LC3B were plated into 96-well plates containing pre-plated siRNA smart pools and transfection reagent (Dharmacon). Cells were fixed 48 hours after plating, stained with Hoechst 33342, and then imaged. Cell boundaries were determined based on nuclear staining with eYFP-positive and mCherry-positive LC3B puncta detected based on pre-set parameters in the iDev software. LC3B acidification was determined by subtracting the ratio of punctate eYFP-LC3B signal (neutral pH) to that of mCherry-LC3B signal (total LC3B) from 2; thus, values closer to 2 have increased delivery of the LC3B reporter to the lysosome while cells with inhibited delivery of LC3B to lysosomes will have reduced values. Those TRIMs whose LC3B acidification had values >3 standard deviations below the mean of cells transfected with non-targeting siRNA were considered hits. >500 cells per siRNA were analyzed in two independent experiments.

## Immunofluorescent staining

For high content imaging, cells were seeded in either 24-well or 96-well plates (2 × 10□ cells per well for a 24-well plate or 1 × 10□ cells per well for a 96-well plate). For confocal experiments, $1 \times 10^5$ cells were plated onto coverslips in 12-well plates. Cells were fixed with 4% paraformaldehyde for 3 minutes and then washed twice with 1 × PBS. In general, permeabilization was performed using 0.2% saponin and 1% BSA in PBS for 30 minutes, but for TFEB staining cells were permeabilized with 0.1% Triton X-100 and 0.1% Tween 20 for 10 minutes, followed by two washes with PBS and blocking with 1% BSA in PBS for 30 minutes. Primary antibodies were applied at the dilutions specified above and incubated with the cells for

1 hour at room temperature. Following two washes with PBS to remove residual primary antibody solution, cells were incubated with appropriate secondary antibodies for 1 hour at room temperature. Samples were then washed twice with 1 × PBS. Coverslips were mounted with ProLong Diamond Antifade mounting media (P36970, Invitrogen), while cells in multi-well plates were left in PBS for high content imaging.

**High content microscopy and analysis**

Following immunofluorescence staining as described above, cells were counterstained with Hoechst 33342 to visualize nuclei. High-content imaging was performed using a Cellomics HCS or CellInsight CX7 instruments and analyzed with iDEV software (Thermo Fisher). Hoechst 33342 nuclear staining was utilized for autofocusing, and regions of interest (ROIs) were defined relative to nuclear positions. Targets were identified based on fluorescence intensity within the ROI, and parameters such as object count, total area, total intensity, average intensity, co-localization area, and correlation coefficient between targets were analyzed on a per-cell basis using automated algorithms.

*Puncta identification and quantitation*, *colocalization analysis*, and *analysis of nuclear localization*: Puncta detection, colocalization, and nuclear localization were analyzed using the Cellomics colocalization BioApplication. Cell boundaries were defined based on either CellMask staining (H32722, Thermofisher) or the nuclei stained with Hoechst 33342 (H3570, Thermofisher). When nuclei were used to define cell boundaries, the nuclear parameter was extended to the surrounding cytoplasmic region. Single-cell segmentation was performed using nuclear intensity-based methods, and nuclei with irregular morphology or insufficient intensity were excluded to minimize segmentation errors. For puncta identification and quantification as well as colocalization analysis, the region of interest (ROI) was set to the cytoplasm, whereas for nuclear localization analysis, only the nuclear ROI was used. Target signals were measured within the defined ROI. Colocalization was quantified by automated calculation of the overlapping area between two target signals. Nuclear localization of TFEB was assessed by measuring the total nuclear intensity of TFEB, and the percentage of cells exceeding predefined nuclear intensity threshold was calculated. *Analysis of trans-Golgi network fragmentation*: Golgi morphology was analyzed using the Morphology Explorer BioApplication. TGN46-postitive structures larger than 3 $\mu m^2$ were classified as coalescent Golgi, whereas structures smaller than 3 $\mu m^2$ were classified as fragmented Golgi. The number of fragmented Golgi per cell was quantified and compared between WT and TRIM46 knockout cells. *Analysis of microtubule*

*organization*: Microtubule organization was quantified using the Cellomics Morphology Explorer Bioapplication. Microtubules were visualized by immunofluorescence staining with α-tubulin (sc-23948, Santa Cruz) as described above. The software classified microtubule structures as either spotted or fibrous based on morphology, and fibers smaller than 0.794 $\mu m^2$ were defined as 'short' microtubules. To assess microtubule organization in TRIM46 knockout cells, the ratio of the total area of short microtubules versus the total microtubule area was calculated and compared to WT. Microtubule bundling was analyzed using the built-in fiber alignment feature of the software. The orientation of individual fibers was determined relative to the image axis, and the standard deviation of fiber angles within a single cell was used as a measure of microtubule alignment. A minimum of 500 cells per well were analyzed, with data from multiple wells per experiment and ≥3 independent experiments pooled for quantitative analysis.

**Confocal microscopy and deconvolution**

Sub-airy unit (0.6AU) pinhole confocal microscopy with a Zeiss LSM900 or a Leica TCS-SP8 microscope was performed followed by computational image restoration with Huygens Essential (Scientific Volume Imaging, Hilversum, Netherlands) utilizing a constrained maximum likelihood estimation algorithm. Images were acquired using 63X/1.4NA plan apochromat oil immersion objective lenses and sampled at ideal Nyquist sampling rates in x, y, and z planes, allowing for sub-diffraction limited resolution following image restoration. All images were rendered on a high performance CUDA-GPA enabled workstation and 3D renders were generated for morphological analysis with Huygens Object Analyzer software. Sphericity values for LC3B-positive structures were obtained using the "RoughSphericity" feature. Colocalization between LC3B and TGN46 was quantified using the colocalization coefficients feature, reporting Pearson's correlation coefficient. In addition, profile intensity plots were generated to visualize the overlap between LC3B and LAMP2 signals.

**Western blot analysis**

Cells were washed twice with PBS and lysed in RIPA buffer (89901, Thermo Fisher) supplemented with protease inhibitors (11836170001, Sigma) and phosphatase inhibitors (PHOSS-RO, Sigma). Protein concentrations were determined using the BCA reagent (23228, Thermo Fisher). Equal amounts of protein were mixed with Laemmli Sample Buffer (1610747, Bio-Rad) and boiled at 100°C for 10 minutes. Denatured proteins were separated on either 4–20%

gradient or 10% SDS-PAGE gels (Bio-Rad) at 95 V and transferred to methanol-activated PVDF membranes or nitrocellulose membranes at 100 V for 1 hour at 4°C. Membranes were blocked with 5% skim milk in PBS and incubated with primary antibodies overnight at 4°C. After three 10-minute washes with PBST (0.1% Tween-20), membranes were incubated with secondary antibodies for 1 hour at room temperature. Following three additional washes with PBST, membranes were developed using ECL substrate (1705061, Bio-Rad) for HRP-conjugated antibodies or directly imaged using a ChemiDoc imager (Bio-Rad) for fluorescent secondary antibodies. Protein quantification was performed using Image Lab software (Bio-Rad).

**Halo LC3 assay for autophagy flux**

HeLa WT or TRIM46 knockout cells stably expressing Halo-LC3 (HT-LC3B) were seeded at a density of $3 \times 10^5$ cells per well in 6-well plates. The following day, cells were pulsed with 2.5µM TMR-labeled HaloTag ligand (HL) for 30 minutes, followed by three washes with DMEM. Cells were then treated with either DMSO or 100 nM Bafilomycin A1 for 4 or 6 hours. After treatment cells were washed twice with PBS and lysed in RIPA buffer supplemented with protease inhibitors. Protein concentrations were determined using a BCA assay, and equal amounts of protein were subjected to SDS-PAGE. Released HT/HL was detected by TMR fluorescence in-gel using a ChemiDoc™ MP Imager (Bio-Rad) prior to immunoblotting for actin.

**DQ-BSA assay**

To assess lysosomal function, cells were seeded in a 96-well plate and incubated overnight with 10 µg/ml DQ-BSA (D12050, Thermo Fisher) diluted in culture medium. Following incubation, cells were fixed with paraformaldehyde prior to immunolabeling with anti-LAMP2 and high content imaging.

**Membrane fractionation**

Membrane fractionation was performed as described previously[69]. Cells from the two 15-cm dishes grown to confluence were harvested and homogenized in 5X cell pellet volume of buffer B1 buffer (20 mM HEPES-KOH, 400 mM sucrose, and 1 mM EDTA) supplemented with protease and phosphatase inhibitors and 0.3 mM DTT by passing through a 22-G needle. Homogenates were subjected to sequential differential centrifugation at 1000 x g for 10 min, 3000 × g for 10 min, 25, 000 × g for 20 min, and 100, 000 × g for 30 minutes to collect the

pelleted membranes. Pellets were lysed in RIPA buffer supplemented with protease inhibitors and protein concentrations were determined using a BCA assay. Samples were mixed with Laemmli Sample Buffer (1610747, Bio-Rad), boiled for 10 minutes, and analyzed by SDS-PAGE and immunoblotting with antibodies against LC3B, LAMP2, and TGN46.

### Flow cytometric measurement of Golgiphagy

HeLa wild-type or TRIM46 knockout cells ($2 \times 10^6$) were seeded in 10 cm dishes one day before transfection. Cells were transfected with 14 µg of the pKH116-Keima-YIPF3 plasmid (214970, Addgene) using Lipofectamine 2000 (Thermo Fisher) according to the manufacturer's protocol. 16 hours post-transfection, the culture medium was replaced with fresh medium. On day 2, cells were starved in Earle's Balanced Salt Solution (EBSS; 24010043, Thermo Fisher) with or without 100 nM bafilomycin A1 for 6 hours. After treatment, cells were harvested by trypsinization and resuspended in PBS containing 5% FBS for flow cytometry analysis. Acidified Golgi structures were assessed using dual-excitation ratiometric pH measurements at 405 nm (neutral pH ~7) and 561 nm (acidic pH ~4) laser excitations, with emission detected at 603/48 nm and 620/15 nm respectively using the flow cytometry (Attune NxT, Thermofisher). Flow cytometry data were acquired and analyzed using FlowJo software (version 10, Tree Star).

### Statistical analysis, graphing and figure assembly

All data are presented as mean ±□s.e.m. Statistical significance between two groups was assessed using a two-sided unpaired Student's *t*-test for normally distributed data or a two-sided Mann-Whitney *U*-test for non-normally distributed data. For multiple group comparison, one-way or two-way Anova followed by Tukey's post hoc test was applied. Statistical analyses and graph generation were conducted using Graphpad Prism v10.6.0. Schematic diagrams were prepared with BioRender, and final figure assembly was performed using Adobe Illustrator.

## KEY RESOURCES

| REAGENT or RESOURCE | SOURCE | IDENTIFIER |
|---|---|---|
| **Antibodies** | | |
| Anti-mCherry antibody | Abcam | ab183628, RRID: AB_2650480 |

| | | |
|---|---|---|
| GABARAP | Abcam | ab109364, RRID: AB_10861928 |
| NPC2 | Abcam | ab218192, RRID: AB_2941808 |
| Purified Mouse Anti-p62 Ick ligand | BD biosciences | P0067, RRID: AB_398151 |
| Goat Anti-Mouse IgG (H+L)-HRP | BIO-RAD | 1721011, RRID: AB_2617113 |
| Goat Anti-Rabbit IgG (H+L)-HRP | BIO-RAD | 1721019, RRID: AB_11125143 |
| TGN46 | BIO-RAD | AHP500G, RRID: AB_2203291 |
| AMPK | Cell Signaling Technology | 2532, RRID: AB_330331 |
| phospho-AMPK T172 | Cell Signaling Technology | 2535, RRID: AB_331250 |
| Atg13 (E1Y9V) Rabbit mAb | Cell Signaling Technology | 13468, RRID: AB_2797419 |
| BECN1 | Cell Signaling Technology | 3459, RRID: AB_560924 |
| GM130 | Cell Signaling Technology | 12480, RRID: AB_2797933 |
| phospho-P70 S6K | Cell Signaling Technology | 9205, RRID: AB_330944 |
| TFEB | Cell Signaling Technology | 4240, RRID: AB_11220225 |
| mTOR | Cell Signaling Technology | 2983, RRID: AB_2105622 |
| ULK1 | Cell Signaling Technology | 8054, RRID: AB_11178668 |
| IRDye® 680LT Goat anti-Mouse IgG Secondary Antibody | LI-COR Biosciences | 925-68020, RRID: AB_2687826 |
| IRDye 800CW Goat anti-Mouse IgG Secondary Antibody | LI-COR Biosciences | 925-32210, RRID: AB_2687825 |
| LC3B | MBL | PM036, RRID: AB_2274121 |
| Anti-Halotag monoclonal antibody | Promega | G921A, RRID:AB_2688011 |
| Cathepsin D | Proteintech | 21327-1-AP, RRID: AB_10733646 |
| LIMP2 | Proteintech | 27102-1-AP, RRID: AB_2880756 |
| TRIM46 | Proteintech | 21026-1-AP, RRID: AB_10732843 |
| Cas9 | Santa Cruz Biotechnology | sc-517386, RRID: AB_2800509 |
| LAMP2 | Santa Cruz Biotechnology | sc-18822, RRID: AB_626858 |
| P70 S6K | Santa Cruz Biotechnology | sc-8418, RRID: AB_628094 |
| Anti-Actin Antibody (2Q1055) | Santa Cruz Biotechnology | sc-58673, RRID: AB_2223345 |
| alpha-tubulin | Santa Cruz Biotechnology | sc-23948, RRID: AB_628410 |
| Rabbit Anti-LC3B | Sigma Aldrich | L7543, RRID: AB_796155 |
| GCP60 | Thermofisher | MA5-25999, RRID: AB_2723827 |
| TGN46 | Thermofisher | MA5-37930, RRID: AB_2897850 |
| WIPI1 | Thermofisher | PA5-34973, RRID: AB_2552322 |
| HCS CellMask™ Near-IR Stain | Thermofisher | H32722 |
| Goat anti-Rabbit IgG (H+L) Highly Cross-Adsorbed Secondary Antibody, Alexa Fluor 488 | ThermoFisher | A-11034, RRID: AB_2576217 |
| Goat anti-Mouse IgG (H+L) Highly Cross-Adsorbed Secondary Antibody, Alexa Fluor Plus 647 | ThermoFisher | A32728, RRID: AB_2633277 |
| **Bacterial and virus strains** | | |

| | | |
|---|---|---|
| NEB 5-alpha Competent E. coli (High Efficiency) | New England Biolabs | C2987 |
| XL10-Gold Ultracompetent cells | Agilent | 210518 |
| **Chemicals, peptides, and recombinant protein** | | |
| 10x Tris/Glycine/SDS buffer | Bio-Rad | 1610732 |
| 2x Laemmli Buffer | Bio-Rad | 1610737 |
| 4x Laemmli Buffer | Bio-Rad | 1610747 |
| Clarity ECL | Bio-Rad | 1705061 |
| Glycine | Bio-Rad | 1610718 |
| Tris Base | Bio-Rad | 1610719 |
| Vinblastine | Cayman chemical | 11762 |
| Vps34-IN1 | Cayman chemical | 17392 |
| Bovine Serum Albumin | Fisher Scientific | CAS 9048-46-8 |
| DTT (Dithiothreitol) | Gold Biotechnology | DTT10 |
| Bafilomycin A1 | Invivogen | tlrl-baf1 |
| HaloTag® TMR Ligand | Promega | G8251 |
| Brefeldin A | Sigma Aldrich | B6542 |
| Ethylenediaminetetraacetic acid disodium salt dihydrate | Sigma Aldrich | E5134 |
| 2-mercaptoethanol | Sigma Aldrich | M3148 |
| Nocodazole | Sigma Aldrich | M1404 |
| PHOSSTOP | Sigma Aldrich | 4906837001 |
| cOmplete™, Mini, EDTA-free Protease Inhibitor Cocktail | Sigma Aldrich | 11836170001 |
| Puromycin dihydrochloride | Sigma Aldrich | P9620 |
| Saponin | Sigma Aldrich | 84510 |
| Sucrose | Sigma Aldrich | 84097 |
| Tween 20 | Sigma Aldrich | P1379 |
| Millipore® Steriflip® Vacuum Tube Top Filter | Sigma Aldrich | SE1M003M00 |
| Dulbecco's modified Eagle's medium | ThermoFisher | 11965084 |
| Earle's Balanced Salt Solution | ThermoFisher | 24010043 |
| fetal bovine serum | ThermoFisher | 26140095 |
| Hoechst 33342 | ThermoFisher | H3570 |
| Lipofectamine 2000 Reagent | ThermoFisher | 11668019 |
| Opti-MEM Reduced Serum Medium | ThermoFisher | 31985070 |
| penicillin-streptomycin | ThermoFisher | 15140122 |
| Restore Plus Western Blot Stripping Buffer | ThermoFisher | 46430 |
| RIPA lysis buffer | ThermoFisher | 89901 |
| Trypsin-EDTA (0.25%), phenol red | ThermoFisher | 25200072 |
| Ampicillin Sodium Salt | VWR | IC19014805 |
| Dimethyl Sulfoxide (DMSO) | VWR | EMMX14586 |
| Ethanol | VWR | 89125172 |
| Kanamycin Sulfate | VWR | 97061-600 |
| Methanol | VWR | BDH20291GLP |

| | | |
|---|---|---|
| Paraformaldehyde | VWR | JTS8987 |
| Potassium Chloride | VWR | EMPX14051 |
| Potassium Phosphate Monobasic | VWR | EMDPX15651 |
| 2-Propanol (Isopropyl Alcohol) | VWR | BDH20271GLP |
| Sodium Chloride | VWR | BDH928625KG |
| Sodium Phosphate Dibasic | VWR | 97061472 |
| Triton X-100 | VWR | EM9410 |
| **Critical commercial assays** | | |
| Agilent QuikChange Lightning Site-Directed Mutagenesis Kit | Agilent | 210518 |
| BCA reagent | ThermoFisher | 23228 |
| Extracta Plus DNA | QuantaBio | 95213-050 |
| Gateway™ BP Clonase™ II Enzyme mix | ThermoFisher | 11789100 |
| Gateway™ LR Clonase™ II Enzyme mix | ThermoFisher | 11791020 |
| Guide-it™ Complete sgRNA Screening System | Takara Bio | 632636 |
| QIAprep Spin Miniprep Kit | Qiagen | 27104 |
| QIAquick PCR Purification Kit | Qiagen | 28106 |
| PureLink™ HiPure Plasmid Midiprep Kit | Thermo Fisher | K210005 |
| ProFection Mammalian Transfection System | Promega | E1200 |
| **Experimental models: Cell lines** | | |
| HeLa TRIM46 knockout | This study | |
| HEK293T TRIM46 knockout | This study | |
| HeLa stably expressing HT-LC3 | This study | |
| HeLa TRIM46 knockout cells stably expressing HT-LC3 | This study | |
| **Oligonucleotides** | | |
| TRIM46 Forward primer for sgRNA | This study | 5'-CCTCTAATACGACTCACTATAGGTACCGTTGAGTTCCGGCGCAGTTTAAGAGCTATGC-3' |
| TRIM46 Forward primer for genomic DNA amplification | This study | 5'-GCTGCTTTCCCTTTTCCT-3' |
| TRIM46 Reverse primer for genomic DNA amplification | This study | 5'-CTCTGAAGTTCAGAGAGGGT-3' |
| TRIM46 Forward primer for site-directed mutagenesis g1407t | This study | 5'-AGTTCCGGCGCACTGATGTGCCTGCTC-3' |
| TRIM46 Reverse primer for site-directed mutagenesis g1407t | This study | 5'-GAGCAGGCACATCAGTGCGCCGGAACT-3' |
| siControl | GE Dharmacon | D-001206-13-05 |
| siATG7 | GE Dharmacon | M-020112-01-005 |
| siATG13 | GE Dharmacon | M-020765-01-0005 |

| | | |
|---|---|---|
| siBECN1 | GE Dharmacon | M-010552-01-0005 |
| siULK1 | GE Dharmacon | M-005049-00-0005 |
| siTRIM1/MID2 | GE Dharmacon | M-007076-01 |
| siTRIM2 | GE Dharmacon | M-006955-00 |
| siTRIM3 | GE Dharmacon | M-006931-00 |
| siTRIM4 | GE Dharmacon | M-007101-00 |
| siTRIM5 | GE Dharmacon | M-007100-00 |
| siTRIM6 | GE Dharmacon | M-007121-01 |
| siTRIM7 | GE Dharmacon | M-007077-01 |
| siTRIM10 | GE Dharmacon | M-006920-01 |
| siTRIM11 | GE Dharmacon | M-007075-00 |
| siTRIM13 | GE Dharmacon | M-006923-00 |
| siTRIM14 | GE Dharmacon | M-010976-00 |
| siTRIM15 | GE Dharmacon | M-007102-01 |
| siTRIM16 | GE Dharmacon | M-012220-01 |
| siTRIM16L | GE Dharmacon | M-023055-01 |
| siTRIM17 | GE Dharmacon | M-006981-01 |
| siTRIM18/MID1 | GE Dharmacon | M-006537-01 |
| siTRIM19/PML | GE Dharmacon | M-006547-01 |
| siTRIM20/MEFV | GE Dharmacon | M-011081-00 |
| siTRIM21 | GE Dharmacon | M-006563-02 |
| siTRIM22 | GE Dharmacon | M-006927-03 |
| siTRIM23 | GE Dharmacon | M-006523-00 |
| siTRIM24 | GE Dharmacon | M-005387-03 |
| siTRIM25 | GE Dharmacon | M-006585-00 |
| siTRIM26/ZNF174 | GE Dharmacon | M-019558-02 |
| siTRIM27 | GE Dharmacon | M-006552-01 |
| siTRIM28 | GE Dharmacon | M-005046-01 |
| siTRIM29 | GE Dharmacon | M-012409-01 |
| siTRIM31 | GE Dharmacon | M-006939-01 |
| siTRIM32 | GE Dharmacon | M-006950-01 |
| siTRIM33 | GE Dharmacon | M-005392-03 |
| siTRIM34 | GE Dharmacon | M-006997-01 |
| siTRIM35 | GE Dharmacon | M-006952-02 |
| siTRIM37 | GE Dharmacon | M-006538-02 |
| siTRIM38 | GE Dharmacon | M-006929-01 |
| siTRIM39 | GE Dharmacon | M-007028-01 |
| siTRIM40 | GE Dharmacon | M-007129-01 |
| siTRIM41 | GE Dharmacon | M-007105-02 |
| siTRIM42 | GE Dharmacon | M-007173-00 |
| siTRIM43 | GE Dharmacon | M-007127-01 |
| siTRIM44 | GE Dharmacon | M-017337-01 |
| siTRIM45 | GE Dharmacon | M-007073-01 |
| siTRIM46 | GE Dharmacon | M-007071-01 |
| siTRIM47 | GE Dharmacon | M-007106-02 |
| siTRIM48 | GE Dharmacon | M-007059-01 |
| siTRIM49 | GE Dharmacon | M-007030-01 |
| siTRIM50 | GE Dharmacon | M-007130-00 |
| siTRIM51 | GE Dharmacon | M-010079-02 |

| | | |
|---|---|---|
| siTRIM52 | GE Dharmacon | M-007095-00 |
| siTRIM54 | GE Dharmacon | M-007032-01 |
| siTRIM55 | GE Dharmacon | M-007092-01 |
| siTRIM56 | GE Dharmacon | M-007079-00 |
| siTRIM58 | GE Dharmacon | M-013985-02 |
| siTRIM59 | GE Dharmacon | M-007172-01 |
| siTRIM60 | GE Dharmacon | M-007153-00 |
| siTRIM61 | GE Dharmacon | M-028281-01 |
| siTRIM62 | GE Dharmacon | M-007010-02 |
| siTRIM63 | GE Dharmacon | M-007093-01 |
| siTRIM64 | GE Dharmacon | M-026740-04 |
| siTRIM65 | GE Dharmacon | M-018490-01 |
| siTRIM66 | GE Dharmacon | M-026772-01 |
| siTRIM67 | GE Dharmacon | M-032288-01 |
| siTRIM68 | GE Dharmacon | M-007007-01 |
| siTRIM71 | GE Dharmacon | M-023459-01 |
| siTRIM72 | GE Dharmacon | M-032293-02 |
| siTRIM73 | GE Dharmacon | M-028896-01 |
| siTRIM74 | GE Dharmacon | M-031736-01 |
| siTRIM76/CMYA5 | GE Dharmacon | M-016373-01 |
| **Recombinant DNA** | | |
| mCherry | Pankiv et al, 2007[70] | |
| mCherry-ATG16L1 | Kumar et al, 2021[71] | |
| pDONR221-hTRIM46 | DNASU | HsCD00862242 |
| mCherry-TRIM46 | This study | N/A |
| Myc-TRIM46 | This study | N/A |
| mKeima-YIPF3 | Addgene | 214970 |
| pLV[CRISPR]-hCas9:T2A:Puro-U6-hTRIM46 | VectorBuilder | VB900138-6978huh |
| pLEX307-Halo LC3 | Javed et al, 2025[72] | |
| **Software and algorithms** | | |
| Prism 8 | GraphPad | N/A |
| Image Lab | BIO-RAD | N/A |
| FlowJo (v10.10.0) | BD Biosciences | N/A |
| iDEV software | ThermoFisher | N/A |
| Huygens Object Analyzer and Colocalization | Scientific Volume Imaging | N/A |
| LASX acquisition software | Leica | N/A |
| BioRender | BioRender.com | N/A |
| ICE software | Synthego | |

1 Zhen, Y., Radulovic, M., Vietri, M. & Stenmark, H. Sealing holes in cellular membranes. *The EMBO journal* **40**, e106922 (2021). https://doi.org/10.15252/embj.2020106922
2 Figueras-Novoa, C., Timimi, L., Marcassa, E., Ulferts, R. & Beale, R. Conjugation of ATG8s to single membranes at a glance. *Journal of cell science* **137** (2024). https://doi.org/10.1242/jcs.261031
3 Deretic, V. *et al.* Membrane atg8ylation in Canonical and Noncanonical Autophagy. *Journal of molecular biology* **436**, 168532 (2024). https://doi.org/10.1016/j.jmb.2024.168532
4 Deretic, V. & Lazarou, M. A guide to membrane atg8ylation and autophagy with reflections on immunity. *The Journal of cell biology* **221** (2022). https://doi.org/10.1083/jcb.202203083
5 Mochida, K. & Nakatogawa, H. ER-phagy: selective autophagy of the endoplasmic reticulum. *EMBO reports* **23**, e55192 (2022). https://doi.org/10.15252/embr.202255192
6 Papadopoulos, C., Kravic, B. & Meyer, H. Repair or Lysophagy: Dealing with Damaged Lysosomes. *Journal of molecular biology* **432**, 231-239 (2020). https://doi.org/10.1016/j.jmb.2019.08.010
7 Nthiga, T. M. *et al.* Regulation of Golgi turnover by CALCOCO1-mediated selective autophagy. *The Journal of cell biology* **220** (2021). https://doi.org/10.1083/jcb.202006128
8 Vargas, J. N. S., Hamasaki, M., Kawabata, T., Youle, R. J. & Yoshimori, T. The mechanisms and roles of selective autophagy in mammals. *Nature reviews. Molecular cell biology* **24**, 167-185 (2023). https://doi.org/10.1038/s41580-022-00542-2
9 Kang, J., Li, C. M., Kim, N., Baek, J. & Jung, Y. K. Non-autophagic Golgi-LC3 lipidation facilitates TFE3 stress response against Golgi dysfunction. *The EMBO journal* **43**, 5085-5113 (2024). https://doi.org/10.1038/s44318-024-00233-y
10 Goodwin, J. M. *et al.* GABARAP sequesters the FLCN-FNIP tumor suppressor complex to couple autophagy with lysosomal biogenesis. *Science advances* **7**, eabj2485 (2021). https://doi.org/10.1126/sciadv.abj2485
11 Lv, B. *et al.* A TBK1-independent primordial function of STING in lysosomal biogenesis. *Molecular cell* **84**, 3979-3996 e3979 (2024). https://doi.org/10.1016/j.molcel.2024.08.026
12 Chen, D., Fearns, A. & Gutierrez, M. G. Mycobacterium tuberculosis phagosome Ca(2+) leakage triggers multimembrane ATG8/LC3 lipidation to restrict damage in human macrophages. *Science advances* **11**, eadt3311 (2025). https://doi.org/10.1126/sciadv.adt3311
13 Campisi, D., Hawkins, N., Bonjour, K. & Wollert, T. The Role of WIPI2, ATG16L1 and ATG12-ATG5 in selective and nonselective autophagy. *Journal of molecular biology*, 169138 (2025). https://doi.org/10.1016/j.jmb.2025.169138
14 Boyle, K. B. *et al.* TECPR1 conjugates LC3 to damaged endomembranes upon detection of sphingomyelin exposure. *The EMBO journal* **42**, e113012 (2023). https://doi.org/10.15252/embj.2022113012
15 Kaur, N. *et al.* TECPR1 is activated by damage-induced sphingomyelin exposure to mediate noncanonical autophagy. *The EMBO journal* **42**, e113105 (2023). https://doi.org/10.15252/embj.2022113105
16 Yamamoto, H., Zhang, S. & Mizushima, N. Autophagy genes in biology and disease. *Nat Rev Genet* **24**, 382-400 (2023). https://doi.org/10.1038/s41576-022-00562-w
17 Nambiar, A. & Manjithaya, R. Driving autophagy - the role of molecular motors. *Journal of cell science* **137** (2024). https://doi.org/10.1242/jcs.260481
18 Durgan, J. & Florey, O. Many roads lead to CASM: Diverse stimuli of noncanonical autophagy share a unifying molecular mechanism. *Science advances* **8**, eabo1274 (2022). https://doi.org/10.1126/sciadv.abo1274

19 Florey, O., Gammoh, N., Kim, S. E., Jiang, X. & Overholtzer, M. V-ATPase and osmotic imbalances activate endolysosomal LC3 lipidation. *Autophagy* **11**, 88-99 (2015). https://doi.org/10.4161/15548627.2014.984277
20 Liu, D. *et al.* STING directly activates autophagy to tune the innate immune response. *Cell death and differentiation* **26**, 1735-1749 (2019). https://doi.org/10.1038/s41418-018-0251-z
21 Durgan, J. *et al.* Non-canonical autophagy drives alternative ATG8 conjugation to phosphatidylserine. *Molecular cell* **81**, 2031-2040 e2038 (2021). https://doi.org/10.1016/j.molcel.2021.03.020
22 Grumati, P. & Dikic, I. Ubiquitin signaling and autophagy. *The Journal of biological chemistry* **293**, 5404-5413 (2018). https://doi.org/10.1074/jbc.TM117.000117
23 Di Rienzo, M., Romagnoli, A., Antonioli, M., Piacentini, M. & Fimia, G. M. TRIM proteins in autophagy: selective sensors in cell damage and innate immune responses. *Cell death and differentiation* **27**, 887-902 (2020). https://doi.org/10.1038/s41418-020-0495-2
24 van Gent, M., Sparrer, K. M. J. & Gack, M. U. TRIM Proteins and Their Roles in Antiviral Host Defenses. *Annual review of virology* **5**, 385-405 (2018). https://doi.org/10.1146/annurev-virology-092917-043323
25 Mandell, M. A., Saha, B. & Thompson, T. A. The Tripartite Nexus: Autophagy, Cancer, and Tripartite Motif-Containing Protein Family Members. *Frontiers in pharmacology* **11** (2020). https://doi.org/10.3389/fphar.2020.00308
26 van Beuningen, S. F. B. *et al.* TRIM46 Controls Neuronal Polarity and Axon Specification by Driving the Formation of Parallel Microtubule Arrays. *Neuron* **88**, 1208-1226 (2015). https://doi.org/10.1016/j.neuron.2015.11.012
27 Hatakeyama, S. TRIM Family Proteins: Roles in Autophagy, Immunity, and Carcinogenesis. *Trends in biochemical sciences* **42**, 297-311 (2017). https://doi.org/10.1016/j.tibs.2017.01.002
28 Sparrer, K. M. J. & Gack, M. U. TRIM proteins: New players in virus-induced autophagy. *PLoS pathogens* **14**, e1006787 (2018). https://doi.org/10.1371/journal.ppat.1006787
29 Mandell, M. A. *et al.* TRIM proteins regulate autophagy and can target autophagic substrates by direct recognition. *Developmental cell* **30**, 394-409 (2014). https://doi.org/10.1016/j.devcel.2014.06.013
30 Kimura, S., Noda, T. & Yoshimori, T. Dissection of the autophagosome maturation process by a novel reporter protein, tandem fluorescent-tagged LC3. *Autophagy* **3**, 452-460 (2007).
31 Klionsky, D. J. *et al.* Guidelines for the use and interpretation of assays for monitoring autophagy (3rd edition). *Autophagy* **12**, 1-222 (2016). https://doi.org/10.1080/15548627.2015.1100356
32 Yim, W. W., Yamamoto, H. & Mizushima, N. A pulse-chasable reporter processing assay for mammalian autophagic flux with HaloTag. *eLife* **11** (2022). https://doi.org/10.7554/eLife.78923
33 Frost, L., Dhingra, A., Reyes-Reveles, J. & Boesze-Battaglia, K. The Use of DQ-BSA to Monitor the Turnover of Autophagy-Associated Cargo. *Methods in enzymology* **587** (2016 Nov 17). https://doi.org/10.1016/bs.mie.2016.09.052
34 M, S. *et al.* A gene network regulating lysosomal biogenesis and function - PubMed. *Science (New York, N.Y.)* **325** (07/24/2009). https://doi.org/10.1126/science.1174447
35 C, S. *et al.* TFEB links autophagy to lysosomal biogenesis - PubMed. *Science (New York, N.Y.)* **332** (06/17/2011). https://doi.org/10.1126/science.1204592
36 Settembre, C. *et al.* A lysosome-to-nucleus signalling mechanism senses and regulates the lysosome via mTOR and TFEB. *The EMBO journal* **31**, 1095-1108 (2012). https://doi.org/10.1038/emboj.2012.32

37 JA, M., Y, C., M, G. & R, P. MTORC1 functions as a transcriptional regulator of autophagy by preventing nuclear transport of TFEB - PubMed. *Autophagy* **8** (2012 Jun). https://doi.org/10.4161/auto.19653
38 A, R.-F. *et al.* The transcription factor TFEB links mTORC1 signaling to transcriptional control of lysosome homeostasis - PubMed. *Science signaling* **5** (06/12/2012). https://doi.org/10.1126/scisignal.2002790
39 Paquette, M. *et al.* AMPK-dependent phosphorylation is required for transcriptional activation of TFEB and TFE3. *Autophagy* **17** (2021 Mar 18). https://doi.org/10.1080/15548627.2021.1898748
40 Shin, H.-J. R. *et al.* AMPK–SKP2–CARM1 signalling cascade in transcriptional regulation of autophagy. *Nature* **534** (2016 Jun 15). https://doi.org/10.1038/nature18014
41 Zoncu, R. *et al.* mTORC1 senses lysosomal amino acids through an inside-out mechanism that requires the vacuolar H(+)-ATPase. *Science* **334**, 678-683 (2011). https://doi.org/10.1126/science.1207056
42 J, J. *et al.* Galectins Control mTOR in Response to Endomembrane Damage - PubMed. *Molecular cell* **70** (04/05/2018). https://doi.org/10.1016/j.molcel.2018.03.009
43 S, C. *et al.* TRIMs and Galectins Globally Cooperate and TRIM16 and Galectin-3 Co-direct Autophagy in Endomembrane Damage Homeostasis - PubMed. *Developmental cell* **39** (10/10/2016). https://doi.org/10.1016/j.devcel.2016.08.003
44 Gosavi, P., Houghton, F. J., McMillan, P. J., Hanssen, E. & Gleeson, P. A. The Golgi ribbon in mammalian cells negatively regulates autophagy by modulating mTOR activity. *Journal of Cell Science* **131** (2018/02/01). https://doi.org/10.1242/jcs.211987
45 Gomes-da-Silva, L. C. *et al.* Recruitment of LC3 to damaged Golgi apparatus. *Cell death and differentiation* **26**, 1467-1484 (2019). https://doi.org/10.1038/s41418-018-0221-5
46 PM, M. *et al.* Golgi-derived CLASP-dependent microtubules control Golgi organization and polarized trafficking in motile cells - PubMed. *Nature cell biology* **11** (2009 Sep). https://doi.org/10.1038/ncb1920
47 Hao, H. *et al.* Golgi-associated microtubules are fast cargo tracks and required for persistent cell migration. *EMBO reports* **21** (2020-01-27). https://doi.org/10.15252/embr.201948385
48 Gao, Y. *et al.* Golgi-associated LC3 lipidation requires V-ATPase in noncanonical autophagy. *Cell Death & Disease 2016 7:8* **7** (2016-08-11). https://doi.org/10.1038/cddis.2016.236
49 Hickey, K. L. *et al.* Proteome census upon nutrient stress reveals Golgiphagy membrane receptors. *Nature* **623**, 167-174 (2023). https://doi.org/10.1038/s41586-023-06657-6
50 Kitta, S. *et al.* YIPF3 and YIPF4 regulate autophagic turnover of the Golgi apparatus. *The EMBO journal* **43**, 2954-2978 (2024). https://doi.org/10.1038/s44318-024-00131-3
51 Florey, O., Kim, S. E., Sandoval, C. P., Haynes, C. M. & Overholtzer, M. Autophagy machinery mediates macroendocytic processing and entotic cell death by targeting single membranes. *Nature Cell Biology* **13** (2011 Oct 16). https://doi.org/10.1038/ncb2363
52 Florey, O., Gammoh, N., Kim, S. E., Jiang, X. & Overholtzer, M. V-ATPase and osmotic imbalances activate endolysosomal LC3 lipidation. *Autophagy* **11** (2015-1-2). https://doi.org/10.4161/15548627.2014.984277
53 Durgan, J. & Florey, O. Many roads lead to CASM: Diverse stimuli of noncanonical autophagy share a unifying molecular mechanism. *Science Advances* **8** (2022-10). https://doi.org/10.1126/sciadv.abo1274
54 Hooper, K. M. *et al.* V-ATPase is a universal regulator of LC3-associated phagocytosis and non-canonical autophagy. *The Journal of cell biology* **221** (2022). https://doi.org/10.1083/jcb.202105112

55 Fischer, T. D., Wang, C., Padman, B. S., Lazarou, M. & Youle, R. J. STING induces LC3B lipidation onto single-membrane vesicles via the V-ATPase and ATG16L1-WD40 domain. *The Journal of cell biology* **219** (2020). https://doi.org/10.1083/jcb.202009128
56 Timimi, L. *et al.* The V-ATPase/ATG16L1 axis is controlled by the V(1)H subunit. *Molecular cell* **84**, 2966-2983 e2969 (2024). https://doi.org/10.1016/j.molcel.2024.07.003
57 Xu, Y. *et al.* A Bacterial Effector Reveals the V-ATPase-ATG16L1 Axis that Initiates Xenophagy. *Cell* **178**, 552-566 e520 (2019). https://doi.org/10.1016/j.cell.2019.06.007
58 Hansen, M. D. *et al.* Hepatitis C virus triggers Golgi fragmentation and autophagy through the immunity-related GTPase M. *Proceedings of the National Academy of Sciences of the United States of America* **114**, E3462-E3471 (2017). https://doi.org/10.1073/pnas.1616683114
59 Yin, Y. *et al.* H5 subtype avian influenza virus induces Golgi apparatus stress response via TFE3 pathway to promote virus replication. *PLoS pathogens* **20**, e1012748 (2024). https://doi.org/10.1371/journal.ppat.1012748
60 Joshi, G., Chi, Y., Huang, Z. & Wang, Y. Abeta-induced Golgi fragmentation in Alzheimer's disease enhances Abeta production. *Proceedings of the National Academy of Sciences of the United States of America* **111**, E1230-1239 (2014). https://doi.org/10.1073/pnas.1320192111
61 Haukedal, H. *et al.* Golgi fragmentation - One of the earliest organelle phenotypes in Alzheimer's disease neurons. *Frontiers in neuroscience* **17**, 1120086 (2023). https://doi.org/10.3389/fnins.2023.1120086
62 Farber-Katz, S. E. *et al.* DNA damage triggers Golgi dispersal via DNA-PK and GOLPH3. *Cell* **156**, 413-427 (2014). https://doi.org/10.1016/j.cell.2013.12.023
63 Gosavi, P., Houghton, F. J., McMillan, P. J., Hanssen, E. & Gleeson, P. A. The Golgi ribbon in mammalian cells negatively regulates autophagy by modulating mTOR activity. *Journal of cell science* **131** (2018). https://doi.org/10.1242/jcs.211987
64 Yang, J. *et al.* TM9SF3 is a Golgi-resident ATG8-binding protein essential for Golgi-selective autophagy. *Developmental cell* (2025). https://doi.org/10.1016/j.devcel.2025.06.017
65 Cross, J. *et al.* Lysosome damage triggers direct ATG8 conjugation and ATG2 engagement via non-canonical autophagy. *The Journal of cell biology* **222** (2023). https://doi.org/10.1083/jcb.202303078
66 Liu, X. & Zheng, X. F. Endoplasmic reticulum and Golgi localization sequences for mammalian target of rapamycin. *Molecular biology of the cell* **18**, 1073-1082 (2007). https://doi.org/10.1091/mbc.e06-05-0406
67 Kaeser-Pebernard, S. *et al.* mTORC1 controls Golgi architecture and vesicle secretion by phosphorylation of SCYL1. *Nature communications* **13**, 4685 (2022). https://doi.org/10.1038/s41467-022-32487-7
68 Liu, G. Y. & Sabatini, D. M. mTOR at the nexus of nutrition, growth, ageing and disease. *Nature reviews. Molecular cell biology* **21**, 183-203 (2020). https://doi.org/10.1038/s41580-019-0199-y
69 Ge, L., Melville, D., Zhang, M. & Schekman, R. The ER-Golgi intermediate compartment is a key membrane source for the LC3 lipidation step of autophagosome biogenesis. *eLife* **2**, e00947 (2013). https://doi.org/10.7554/eLife.00947
70 Pankiv, S. *et al.* p62/SQSTM1 binds directly to Atg8/LC3 to facilitate degradation of ubiquitinated protein aggregates by autophagy. *The Journal of biological chemistry* **282**, 24131-24145 (2007).
71 Kumar, S. *et al.* Mammalian hybrid pre-autophagosomal structure HyPAS generates autophagosomes. *Cell* **184**, 5950-5969 e5922 (2021). https://doi.org/10.1016/j.cell.2021.10.017

72 Javed, R. *et al.* Mammalian ATG8 proteins maintain autophagosomal membrane integrity through ESCRTs. *The EMBO journal* **42**, e112845 (2023). https://doi.org/10.15252/embj.2022112845

## FIGURE LEGENDS

### Figure 1. TRIM46 regulates non-degradative LC3 lipidation.

**(A)** siRNA screen for TRIMs regulating the accumulation of non-acidified LC3B. HeLa cells stably expressing mCherry-eYFP-LC3B were transfected with TRIM or control siRNA two days prior to fixation and high content imaging. Neutral pH LC3B puncta (eYFP positive; blue mask) or total LC3B puncta (yellow mask) were identified and quantitated from >500 cells per siRNA. White mask, nuclei; magenta mask, cell boundary. **(B)** TRIM knockdowns (red data points) with LC3B acidification reduced by more than three standard deviations (3X SD) below the mean of non-targeting siRNA controls (blue data points) were identified as hits. Magenta numbers indicate TRIMs 'hits' that were identified in two out of two experiments (see also Figure S1A). **(C–D)** High-content imaging analysis of LC3B abundance in WT and two independent TRIM46 knockout clones. Each dot represents the average LC3B puncta area from >500 cells. **(E, F)** Immunoblot analysis of LC3B-II levels in TRIM46 knockout cells. Quantification of LC3B-II from 3 independent experiments. **(G, H)** Halo-LC3 assay for autophagy flux. WT and TRIM46 knockout cells stably expressing HT-LC3B were pulsed with TMR-HL for 30 minutes prior to 6 h chase with full media. HT/HL were detected by in-gel fluorescence. LE, long exposure. Quantitation (H) shows the percent of total HT/HL signal that results from the "released" HT/HL, a product of lysosomal degradation. **(I, J)** High-content imaging analysis of LC3B (cyan) and LAMP2 (magenta) localization in WT and two TRIM46 knockout clones. Each data point in (J) represents the average area of LC3B and LAMP2 overlap per cell from >500 cells. **(K-M)** Immunoblot analysis of LC3B-II and SQSTM1 abundance in lysates from WT or TRIM46 knockout HeLa cells treated with DMSO or 100 nM bafilomycin A1 (BafA1) for 6 hours. Plots show quantification of relative protein abundance of SQSTM1 (L) and LC3B-II (M). Each dot represents an independent experiment. Data: mean ± SEM; *, $p < 0.05$; ***, $p < 0.001$; ****, $p < 0.0001$; ns, not significant.

### Figure 2. TRIM46 deficiency increases lysosome biogenesis.

**(A, B)** High-content imaging analysis of LAMP2 abundance in WT HeLa and two TRIM46 knockout clones. The average area of punctate LAMP2 per cell from >500 cells was quantitated and graphed in (B). **(C, D)** The levels of the indicated proteins in WT and TRIM46 knockout cells were measured by immunoblotting (C) with quantitation from 6 independent experiments shown in (D). **(E, F)** High content image analysis of TFEB localization in WT and TRIM46 knockout HeLa cells. The percentage of cells showing nuclear-localized TFEB was plotted in (F). Each

data point represents the average calculated from >500 cells. **(G-I)** Immunoblot analysis of the effects of TRIM46 deficiency on mTORC1 and AMPK kinase activity. Quantification of relative protein abundance of phospho-AMPKα (T172) and phospho-P70-S6K (T389) are shown in (H) and (I), respectively. Each data point represents an independent experiment. Data: mean ± SEM; *, $p < 0.05$; **, $p < 0.01$; ***, $p < 0.001$; ****, $p < 0.0001$.

**Figure 3. TRIM46 deficiency triggers microtubule disorganization and Golgi fragmentation.**

**(A-C)** High-content imaging analysis of microtubule organization in WT and TRIM46 knockout (shown, KO #4) HeLa cells. WT and TRIM46 knockout HeLa cells were fixed and stained with anti-α-tubulin antibodies. **(A)** Short (α-tubulin structures < 0.794 $\mu m^2$; cyan mask) and long (α-tubulin structures > 0.794 $\mu m^2$; yellow mask) microtubule structures were automatically segmented. **(B)** The relative abundance of short microtubules per cell was quantified as a percentage of total microtubules and compared between WT and of TRIM46 knockout cells. **(C)** The standard deviation of angles of long microtubule fibers, a measure of microtubule disorganization, was calculated per cell, and the mean values were compared between WT and TRIM46 knockout cells. **(D)** Maximum image projection confocal images of WT and TRIM46 knockout HeLa cells stained with trans-Golgi marker TGN46 and cis-Golgi marker GM130. **(E, F)** High-content imaging analysis of trans-Golgi network (TGN) fragmentation in WT and TRIM46 knockout cells. Representative images are in Supplementary Figure S3B. TGN fragmentation was quantified by determining the number of “small” TGN46-positive structures (<3 $\mu m^2$) per cell (E). The total area of TGN46-positivity per cells was quantitated and plotted relative to what is seen in WT cells (F). Each data point represents the average of >500 cells. Data: mean ± SEM; **, $p < 0.01$, ****; $p < 0.0001$.

**Figure 4. TRIM46 knockout induces Golgi atg8ylation.**

**(A)** Confocal analysis of colocalization between LC3B and TGN46 in WT and TRIM46 knockout (shown, KO #4) HeLa cells. Zoomed in images of the boxed regions are shown below. Arrows indicate colocalized signal. **(B)** Colocalization between TGN46 and LC3B was quantified using Pearson’s correlation coefficient analysis. Each point represents data from a different confocal image. **(C-F)** High content image analysis of WT and TRIM46 knockout HeLa cells stained with

antibodies against GABARAP and TGN46. The average abundance of GABARAP puncta, TGN46 area, and GABARAP/TGN46 overlap area were quantified per cell. Data points represent biological replicates, each based on an average of >500 cells. **(G)** Confocal analysis of mCherry-ATG16L1 and TGN46 localization in transiently transfected TRIM46 knockout cells. Small arrows indicate colocalizing puncta. An enlarged image of the boxed region is shown. The large arrow indicates the path of the measured intensity profile. Data: mean ± SEM; *, $p < 0.05$; **, $p < 0.01$; ***, $p < 0.001$; ****, $p < 0.0001$.

**Figure 5. Enhanced atg8ylation in TRIM46 knockout is independent of canonical autophagy factors.**

**(A-B)** WT or TRIM46 knockout HeLa cells were treated with 10 μM of VPS34-IN1 for 4 hours prior to lysis and immunoblotting (A). Graph (B) shows the relative reduction, expressed as a percent, in LC3-II abundance following VPS34-IN1 treatment. Data points represent independent experiments. **(C-D)** WT or TRIM46 knockout HeLa cells were transfected with the indicated siRNA prior to lysis, immunoblotting (C), and quantitation of LC3B-II levels relative to that seen in WT cells (D). Data points represent independent experiments. **(E-G)** Representative high content images of TRIM46 knockout HeLa cells transfected with the indicated siRNA and stained with antibodies recognizing LC3 and TGN46. Plots show the abundance of punctate LC3B area per cells (F) and the overlapping area between TGN46 and LC3B (G). **(H)** Left, immunoblot analysis of the effect of VPS34-IN1 and BafA1 on LC3B lipidation in WT and TRIM46 knockout cells. Cells were treated with inhibitors (VPS34-IN1: 10 μM, BafA1: 100 nM) or DMSO vehicle control for 4h. Plot (right) shows the abundance of LC3B-II relative to that seen in DMSO-treated WT cells. **(I)** Representative images showing TFEB staining in TRIM46 knockout HeLa cells after transfection with control or ATG7 siRNA. Graph shows the percentage of cells with nuclear TFEB localization as determine by high content imaging. **(J)** Impact of ATG7 knockdown on TGN46 area in TRIM46 knockout cells. Data: mean ± SEM; *, $p < 0.05$; **, $p < 0.01$; ***, $p < 0.001$; ****, $p < 0.0001$; ns, not significant. Data points represent biological replicates, each based on an average of more than 500 cells for microscopy experiments.

**Figure 6. Microtubule disruption phenocopies TRIM46 deficiency, triggering Golgi atg8ylation and increased lysosomal biogenesis.**

WT HeLa cells were treated with 100 nM of Vinblastine for 16 hours. **(A-B)** High-content imaging analysis of TGN fragmentation measured by counting TGN46-positive fragments smaller than 3 μm² (cyan mask). Magenta mask indicates TGN46-positive structures with surface areas >3 μm². **(C)** Confocal microscopic analysis of TGN46 and LC3B colocalization in HeLa cells treated with Nocodazole, Vinblastine, or DMSO control. Arrows indicate colocalizes structures. Insets show magnified images of the area within the dashed-line boxes. **(D-F)** Representative high-content microscopy images of TGN46 and LC3B colocalization following vinblastine treatment. Plots show coalesced LC3-positive area per cell (E), and overlapping area between TGN46 and LC3B (F). **(G-H)** High-content imaging analysis of WT HeLa cells of LAMP2 abundance following vinblastine treatment. **(I-J)** High content imaging analysis of TFEB nuclear localization following vinblastine treatment. **(K)** Model of TRIM46 role in maintaining microtubule organization. Left panel, TRIM46 localizes to microtubules and maintains the organization of microtubule fibers. Right panel, in the absence of TRIM46, microtubules are less organized, leading to Golgi fragmentation and mTORC1 inactivation. In response, v-ATPase subunits are assembled on Golgi-membranes, triggering atg8ylation. Atg8ylation of the Golgi helps restore Golgi architecture and promotes TFEB activation and lysosomal biogenesis. Data: mean ± SEM; ****, $p < 0.0001$. Each data point represents the average of more than 500 cells.

## SUPPLEMENTARY FIGURE LEGENDS

### Supplementary Figure S1. Confirmation of TRIM46 knockout in HeLa and HEK293T cells.

**(A)** A replicate of the experiment shown in Figure 1B. Numbers indicate TRIMs that were >3 standard deviations (line) below the mean measured for non-targeting siRNA (blue data points). Numbers in magenta were 'hits' in two out of two experiments. **(B)** Schematic diagram of the CRISPR confirmation assay. Genomic DNA was extracted, and PCR fragments containing the CRISPR/Cas9 target site in TRIM46 were amplified and incubated with Cas9/sgRNA complexes. Cleavage of unedited DNA generates characteristic fragment sizes, but edited DNA lacks the cleavage site, thus enabling confirmation of CRISPR/Cas9-mediated editing. **(C)** Agarose gel images of HeLa (left) and HEK293T (right) cells confirming TRIM46 knockout via Cas9/sgRNA cleavage of PCR fragments. In WT cells, intact TRIM46 alleles were cleaved by Cas9/sgRNA, generating two fragments (204 bp and 407 bp). In TRIM46 knockout cells, disruption of the cleavage site prevents further cutting, resulting in a single 611 bp fragment. **(D)** Immunoblot analysis of LC3B-II abundance in WT and TRIM46 knockout HEK293T cells. **(E, F)** Immunoblot analysis of LC3B-II abundance in TRIM46 knockout cells transfected with myc-TRIM46 or control vectors. Quantification of LC3B-II from 4 independent experiments. **(G, H)** Maximum image projection confocal micrographs of WT and TRIM46 knockout HeLa cell lines stained with anti-LC3B and anti-LAMP2 antibodies. A zoomed-in image of the boxed region is shown below. Arrow designates the path of intensity profile measurements (plots, bottom). Plot (H) shows the Pearson's correlation coefficient from images in G. Each point represents data from a different confocal image. **(I)** WT and TRIM46 knockout cells expressing Halo-LC3B were pulsed with TMR-labeled HL for 3 minutes prior to a 6-hour chase in full media in the presence or absence of BafA1. HT/HL-LC3B was detected by in-gel fluorescence and actin detected by immunoblot. Plot shows the abundance of HT/HL-LC3B-II in BafA1-treated cells relative to that in cells treated with DMSO vehicle only. Data: mean ± SEM; **, $P < 0.01$; ****, $p < 0.0001$.

### Supplementary Figure S2. Lysosomal biogenesis is increased in TRIM46-knockout cells.

**(A, B)** Immunoblot analysis of lysosomal protein abundance in WT and TRIM46 knockout HEK293T cells. Plots (B) show quantification of the indicated protein's abundance relative to WT. Each data point represents an independent experiment. **(C-E)** DQ-BSA assay for

lysosomal function. WT and TRIM46 knockout HeLa cells were treated with 10 μg/mL DQ-BSA for 6 hours prior to fixation and high-content imaging. Plots show the DQ-BSA intensity per cell (D), and ratio of DQ-BSA intensity to LAMP2 area per cell (E). Each data point represents the average calculated from >500 cells. **(F)** Maximum image projections of confocal images showing LAMP2 and mTOR staining in WT and TRIM46 knockout HeLa cells. The area in the box is enlarged and shown in the microscopy image to the right. Arrow shows the track of the intensity profile measurements (plots, right). **(G)** Colocalization between mTOR and LAMP2 analyzed using Pearson's correlation coefficient. Each point represents data from a different confocal image. Data: mean ± SEM; *, $p < 0.05$; **, $p < 0.01$; ns, not significant.

**Supplementary Figure S3. Microtubule-localizing TRIM46 regulates TGN architecture without increasing the abundance of Golgi-related proteins.**

**(A)** Maximum image projection confocal images of HeLa cells transfected with mCherry-TRIM46 and stained for α-tubulin. **(B)** Representative high-content microscopy images of WT and TRIM46 knockout HeLa cells stained with TGN46 related to Figure 3E and 3F. Magenta mask illustrates "large" TGN46 structures (>3 $\mu m^2$) and cyan mask highlights fragmented TGN46 structures (<3 $\mu m^2$). **(C)** Immunoblot analysis of the abundance of selected Golgi-resident proteins in WT and TRIM46 knockout HeLa cells. Plots show quantification of relative protein levels in TRIM46 knockout cells compared to WT. Dots represents independent experiments. Data: mean ± SEM; ns, not significant.

**Supplementary Figure S4. TRIM46 knockout cells show increased non-degradative atg8ylation of the trans-Golgi network (TGN).**

**(A, B)** High content imaging analysis of colocalized LC3B and TGN46 in WT and two TRIM46 knockout clones. Data points represent three independent experiments, each based on an average of >500 cells. **(C, D)** Confocal microscopy analysis of the morphology of structures showing overlapping TGN46/LC3B signal. Top, maximum image projection of a TRIM46-knockout HeLa cell. Three dimensional reconstructions of the boxed structures are shown below. Violin plot (D) showing the sphericity of LC3B-positive structures quantitated from confocal images of WT and TRIM46 knockout HeLa cells. Thick bars, media; thin bars, quartiles. Perfectly spherical objects will have a value of 1. **(E)** Gradient centrifugation of

membrane fractions isolated from WT and TRIM46 knockout cells. **(F-H)** High content imaging analysis of TGN46 and ATG16L1 colocalization in WT or TRIM46 knockout HeLa cells. Cells were transfected with mCherry-ATG16L1 and stained with TGN46. Masks in bottom image: yellow, TGN46 positive; red, ATG16L1 positive. Graphs show the abundance of overlapping (E) and the Pearson's correlation coefficient ATG16L1/TGN46 colocalization (F) on a per-cell basis. Each data point represents the average of >500 cells. **(I)** Flow cytometric analysis of the delivery of the Golgiphagy reporter YIPF3-mKeima to lysosomes in WT and TRIM46 knockout cells. WT HeLa cells were starved in EBSS for 6 hours with or without 100 nM BafA1 as controls. One representative experiment of two was shown. Data: mean ± SEM; *, $p < 0.05$; **, $p < 0.01$; ****, $p < 0.0001$.

**Supplementary Figure S5. ATG7, but not ATG13, is required for atg8ylation in TRIM46 knockout cells.**

**(A, D)** Representative images of WT and TRIM46 knockout HeLa cells transfected with siRNAs targeting ATG7 (A) or ATG13 (D), stained with antibodies against LC3B and TGN46. Plots show quantification of LC3 puncta area per cell **(B, E)** and colocalized LC3B and TGN46 signal **(C, F)**. Data points represent biological replicates, each based on an average of more than 500 cells. **(G)** Western blot confirming ATG7 or ATG13 knockdown efficiency. Data: mean ± SEM; *, $p < 0.05$; **, $p < 0.01$; ***, $p < 0.001$.

**Supplementary Figure S6. Microtubule disruption with nocodazole triggers atg8ylation of Golgi fragments and increased lysosomal biogenesis.**

WT HeLa cells were treated with 100 nM nocodazole or DMSO control for 16 hours. **(A-B)** High-content imaging analysis of TGN fragmentation measured by counting small TGN46-positive structures (cyan mask) smaller than 3 $\mu m^2$. Larger TGN46-positive structures are labeled with the magenta mask. **(C-E)** Representative high-content microscopy images of TGN46 (magenta) and LC3 (cyan) colocalization following nocodazole treatment. Plots show quantitation of LC3B puncta area per cell (D) and overlapping area between TGN46 and LC3B (E). **(F, G)** High content imaging analysis of WT HeLa cells measuring LAMP2 abundance following nocodazole or DMSO control treatment. **(H, I)** High content imaging analysis of TFEB nuclear localization following nocodazole or control treatment of HeLa cells. **(J-P)** High content

image analysis of Golgi fragmentation (J, K), LC3B puncta abundance (L, M), TGN46/LC3B colocalization (L, N) and TFEB nuclear localization (O, P) in HeLa cells treated or not with brefeldin A (BrefA) for 16 hours. Each data point represents the average of more than 500 cells. Data: mean ± SEM; ****, $p < 0.0001$.

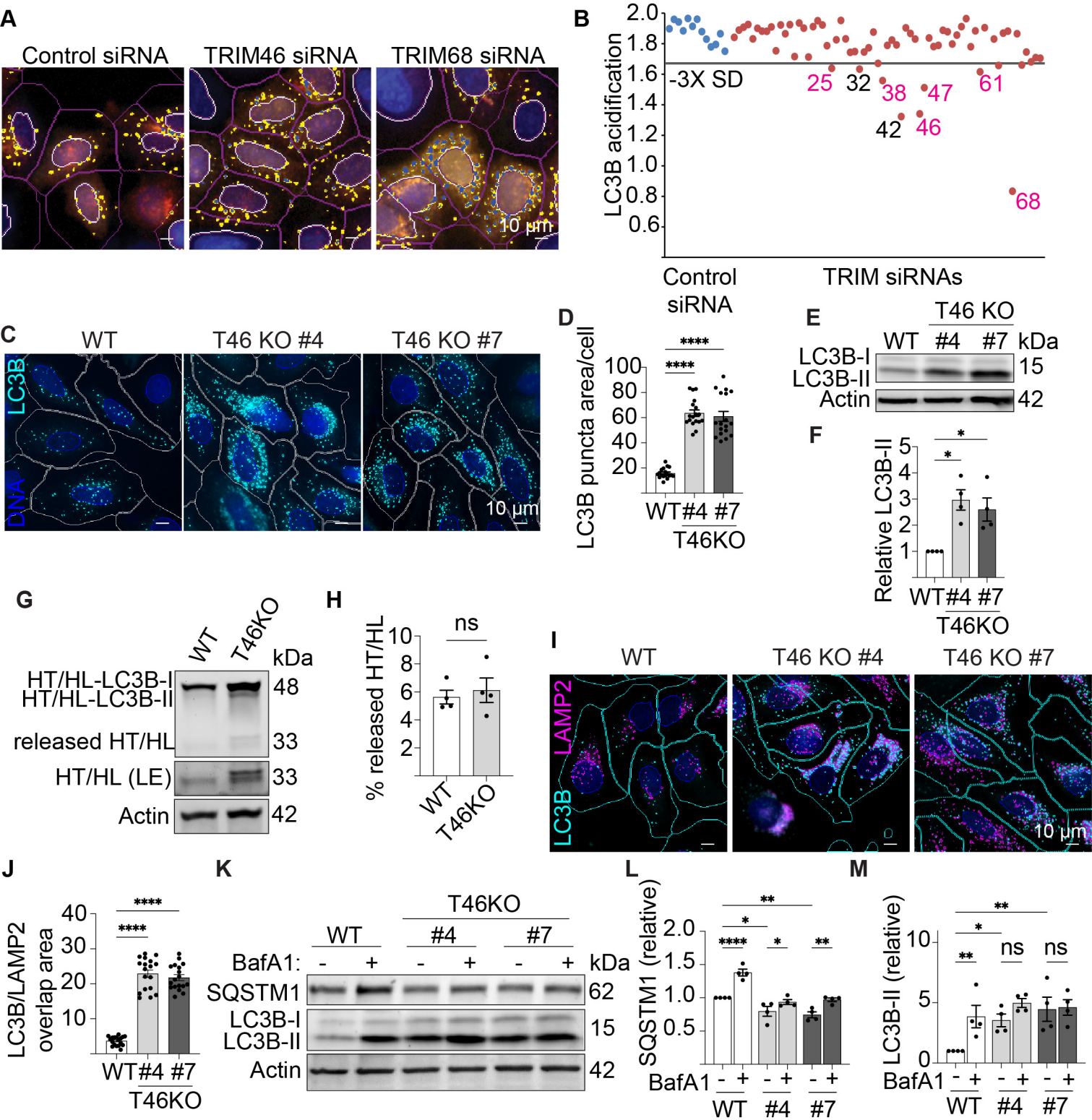
A
Control siRNA
TRIM46 siRNA
TRIM68 siRNA
10 µm
B
LC3B acidification
-3X SD
25
32
38
47
61
42
46
68
Control siRNA
TRIM siRNAs
C
WT
T46 KO #4
T46 KO #7
LC3B
DNA
10 µm
D
LC3B puncta area/cell
****
****
WT
#4
#7
T46KO
E
T46 KO
WT
#4
#7
kDa
LC3B-I
LC3B-II
Actin
15
42
F
Relative LC3B-II
*
*
WT
#4
#7
T46KO
G
WT
T46KO
kDa
HT/HL-LC3B-I
HT/HL-LC3B-II
48
released HT/HL
33
HT/HL (LE)
33
Actin
42
H
% released HT/HL
ns
WT
T46KO
I
WT
T46 KO #4
T46 KO #7
LAMP2
LC3B
10 µm
J
LC3B/LAMP2 overlap area
****
****
WT
#4
#7
T46KO
K
T46KO
WT
#4
#7
BafA1:
kDa
SQSTM1
LC3B-I
LC3B-II
Actin
62
15
42
L
SQSTM1 (relative)
**
*
****
*
**
BafA1
WT
#4
#7
M
LC3B-II (relative)
**
*
**
ns
ns
BafA1
WT
#4
#7

**Figure 1**

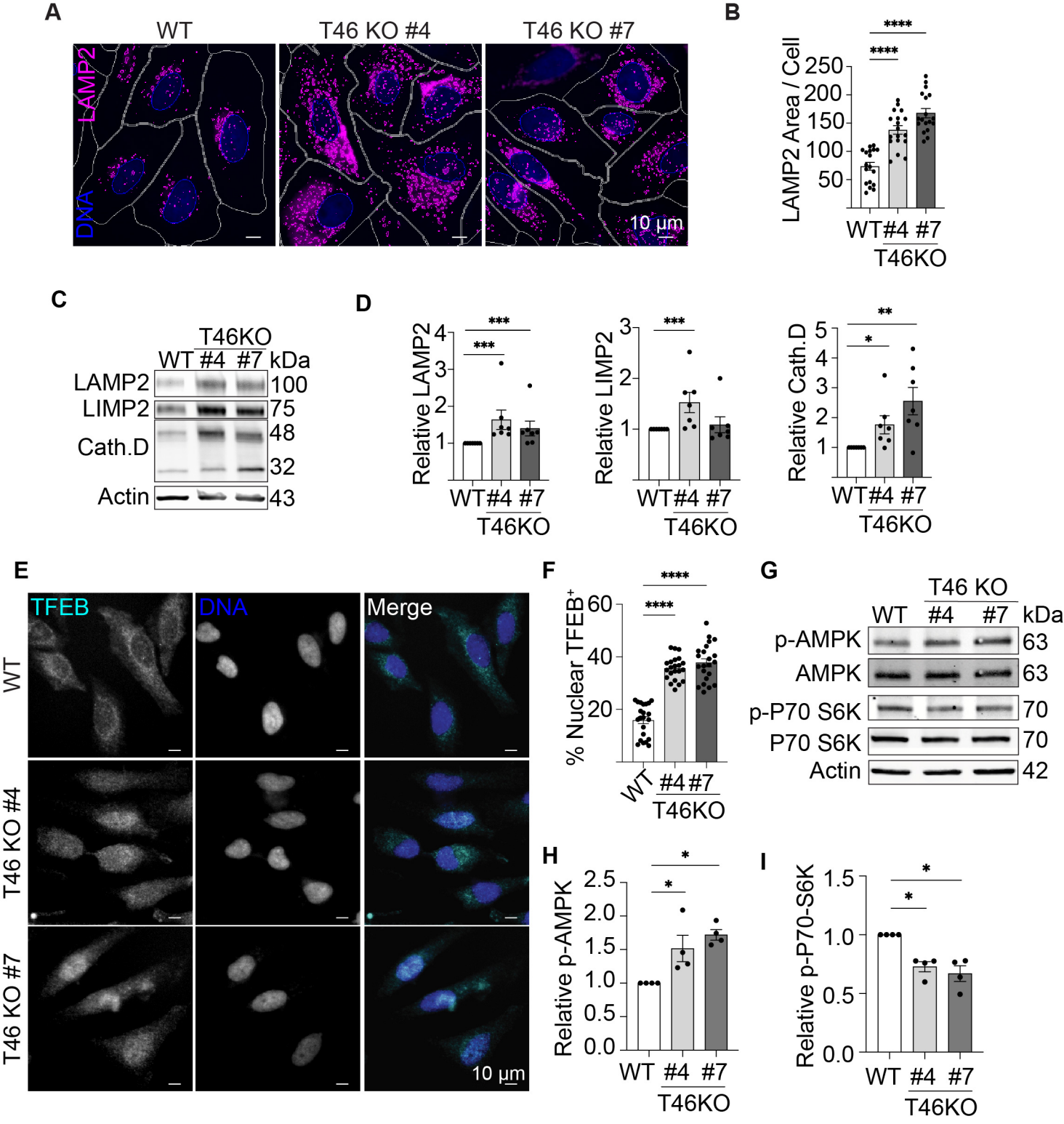
A
WT
T46 KO #4
T46 KO #7
LAMP2
DNA
10 µm
B
LAMP2 Area / Cell
250
200
150
100
50
****
****
WT #4 #7
T46KO
C
T46KO
WT #4 #7 kDa
LAMP2 100
LIMP2 75
Cath.D 48
32
Actin 43
D
Relative LAMP2
Relative LIMP2
Relative Cath.D
***
***
*
**
WT #4 #7
T46KO
E
TFEB
DNA
Merge
WT
T46 KO #4
T46 KO #7
10 µm
F
% Nuclear TFEB+
60
40
20
****
****
WT #4 #7
T46KO
G
T46 KO
WT #4 #7 kDa
p-AMPK 63
AMPK 63
p-P70 S6K 70
P70 S6K 70
Actin 42
H
Relative p-AMPK
2.5
2.0
1.5
1.0
0.5
0.0
*
*
WT #4 #7
T46KO
I
Relative p-P70-S6K
1.5
1.0
0.5
0.0
*
*
WT #4 #7
T46KO

**Figure 2**

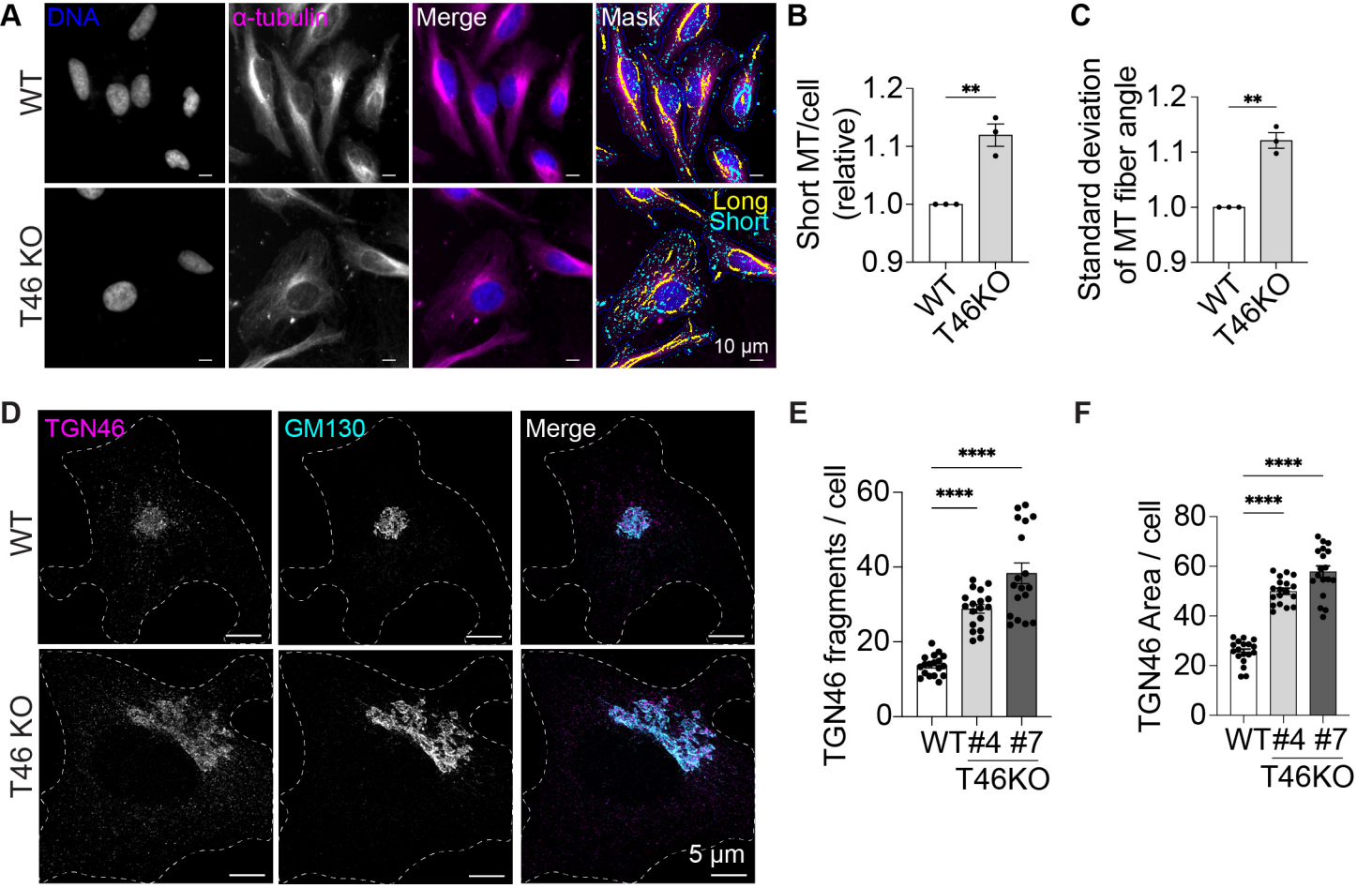
A
DNA
α-tubulin
Merge
Mask
WT
T46 KO
Long
Short
10 µm
B
Short MT/cell (relative)
1.2
1.1
1.0
0.9
**
WT
T46KO
C
Standard deviation of MT fiber angle
1.2
1.1
1.0
0.9
**
WT
T46KO
D
TGN46
GM130
Merge
WT
T46 KO
5 µm
E
TGN46 fragments / cell
60
40
20
0
****
****
WT
#4
#7
T46KO
F
TGN46 Area / cell
80
60
40
20
0
****
****
WT
#4
#7
T46KO

**Figure 3**

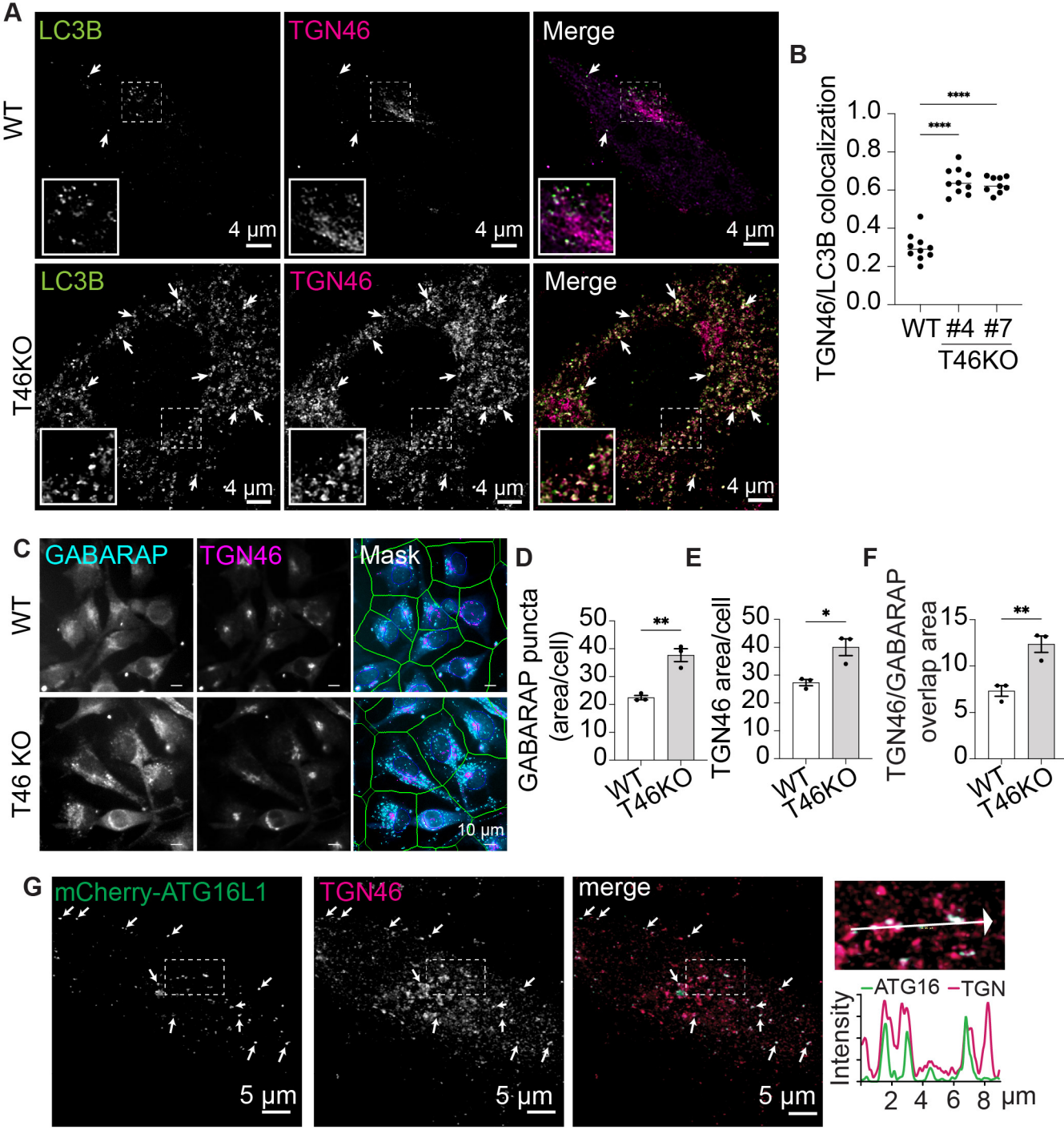
A
LC3B
TGN46
Merge
WT
T46KO
4 µm
B
TGN46/LC3B colocalization
1.0
0.8
0.6
0.4
0.2
0.0
****
****
WT
#4
#7
T46KO
C
GABARAP
TGN46
Mask
WT
T46 KO
10 µm
D
GABARAP puncta (area/cell)
50
40
30
20
10
0
**
WT
T46KO
E
TGN46 area/cell
*
F
TGN46/GABARAP overlap area
15
5
G
mCherry-ATG16L1
merge
5 µm
ATG16
TGN
Intensity
2
4
6
8
µm

Figure 4

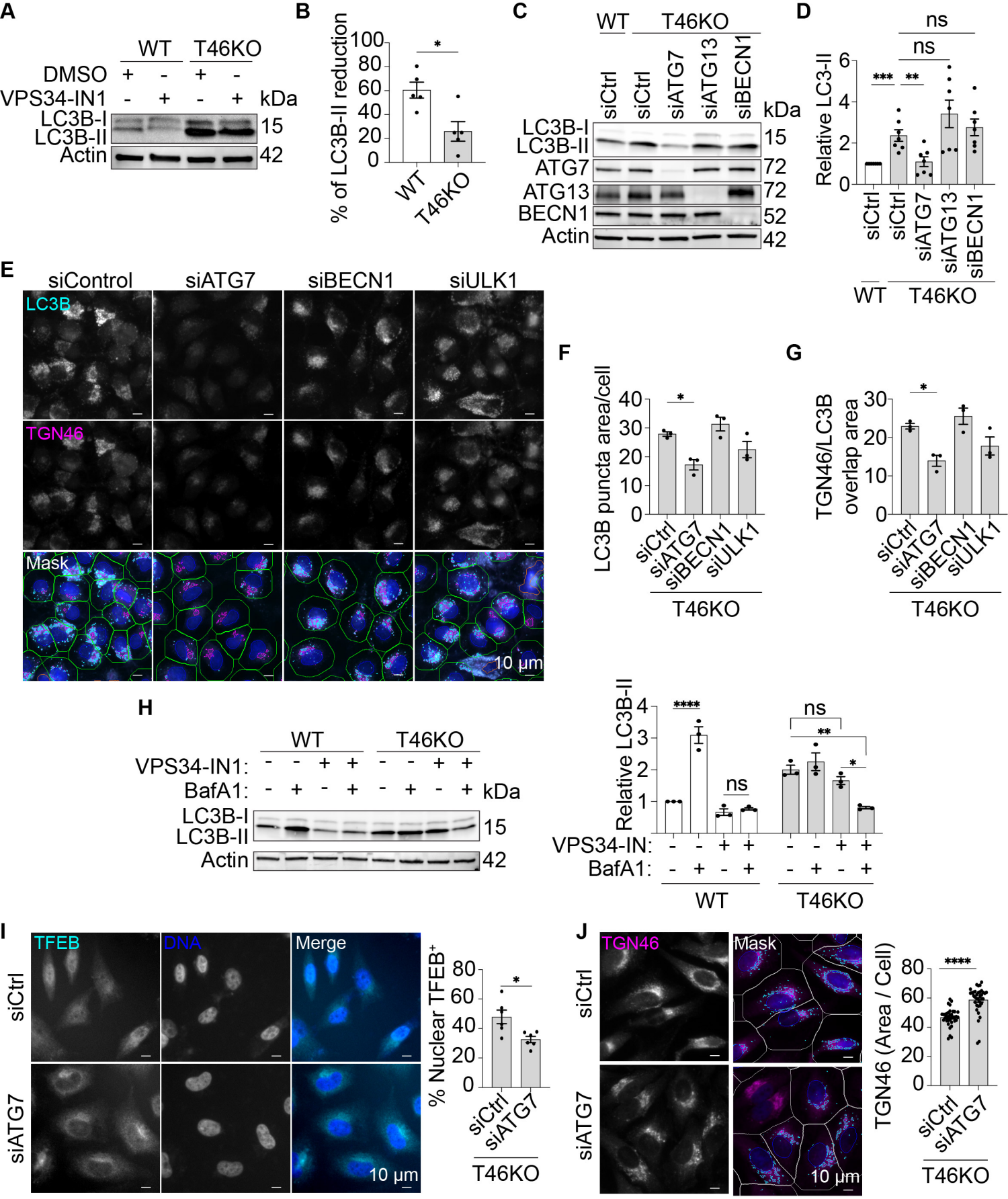
A
WT
T46KO
DMSO
VPS34-IN1
kDa
LC3B-I
LC3B-II
Actin
15
42
B
% of LC3B-II reduction
WT
T46KO
C
WT
T46KO
siCtrl
siCtrl
siATG7
siATG13
siBECN1
kDa
LC3B-I
LC3B-II
ATG7
ATG13
BECN1
Actin
15
72
72
52
42
D
ns
ns
Relative LC3-II
siCtrl
siCtrl
siATG7
siATG13
siBECN1
WT
T46KO
E
siControl
siATG7
siBECN1
siULK1
LC3B
TGN46
Mask
10 µm
F
LC3B puncta area/cell
siCtrl
siATG7
siBECN1
siULK1
T46KO
G
TGN46/LC3B overlap area
siCtrl
siATG7
siBECN1
siULK1
T46KO
H
WT
T46KO
VPS34-IN1:
BafA1:
kDa
LC3B-I
LC3B-II
Actin
15
42
Relative LC3B-II
ns
ns
VPS34-IN:
BafA1:
WT
T46KO
I
TFEB
DNA
Merge
siCtrl
siATG7
10 µm
% Nuclear TFEB+
siCtrl
siATG7
T46KO
J
TGN46
Mask
siCtrl
siATG7
10 µm
TGN46 (Area / Cell)
siCtrl
siATG7
T46KO

**Figure 5**

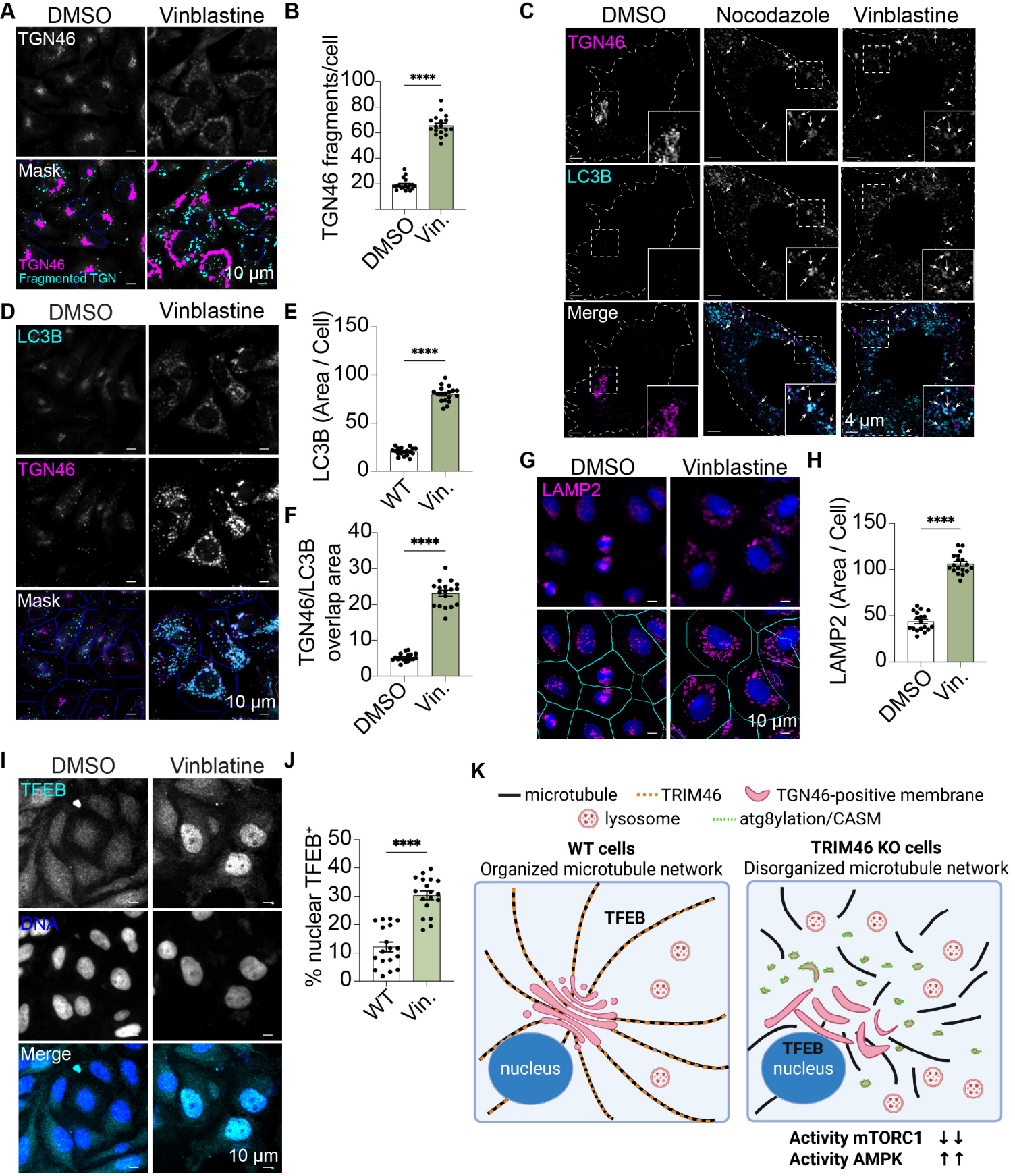
A
DMSO
Vinblastine
TGN46
Mask
TGN46
Fragmented TGN
10 µm
B
TGN46 fragments/cell
100
80
60
40
20
****
DMSO
Vin.
C
DMSO
Nocodazole
Vinblastine
TGN46
LC3B
Merge
4 µm
D
DMSO
Vinblastine
LC3B
TGN46
Mask
10 µm
E
LC3B (Area / Cell)
150
100
50
0
****
WT
Vin.
F
TGN46/LC3B overlap area
40
30
20
10
0
****
DMSO
Vin.
G
DMSO
Vinblastine
LAMP2
10 µm
H
LAMP2 (Area / Cell)
150
100
50
0
****
DMSO
Vin.
I
DMSO
Vinblatine
TFEB
DNA
Merge
10 µm
J
% nuclear TFEB+
50
40
30
20
10
0
****
WT
Vin.
K
microtubule
TRIM46
TGN46-positive membrane
lysosome
atg8ylation/CASM
WT cells
Organized microtubule network
TRIM46 KO cells
Disorganized microtubule network
TFEB
nucleus
TFEB
nucleus
Activity mTORC1 ↓↓
Activity AMPK ↑↑

**Figure 6**

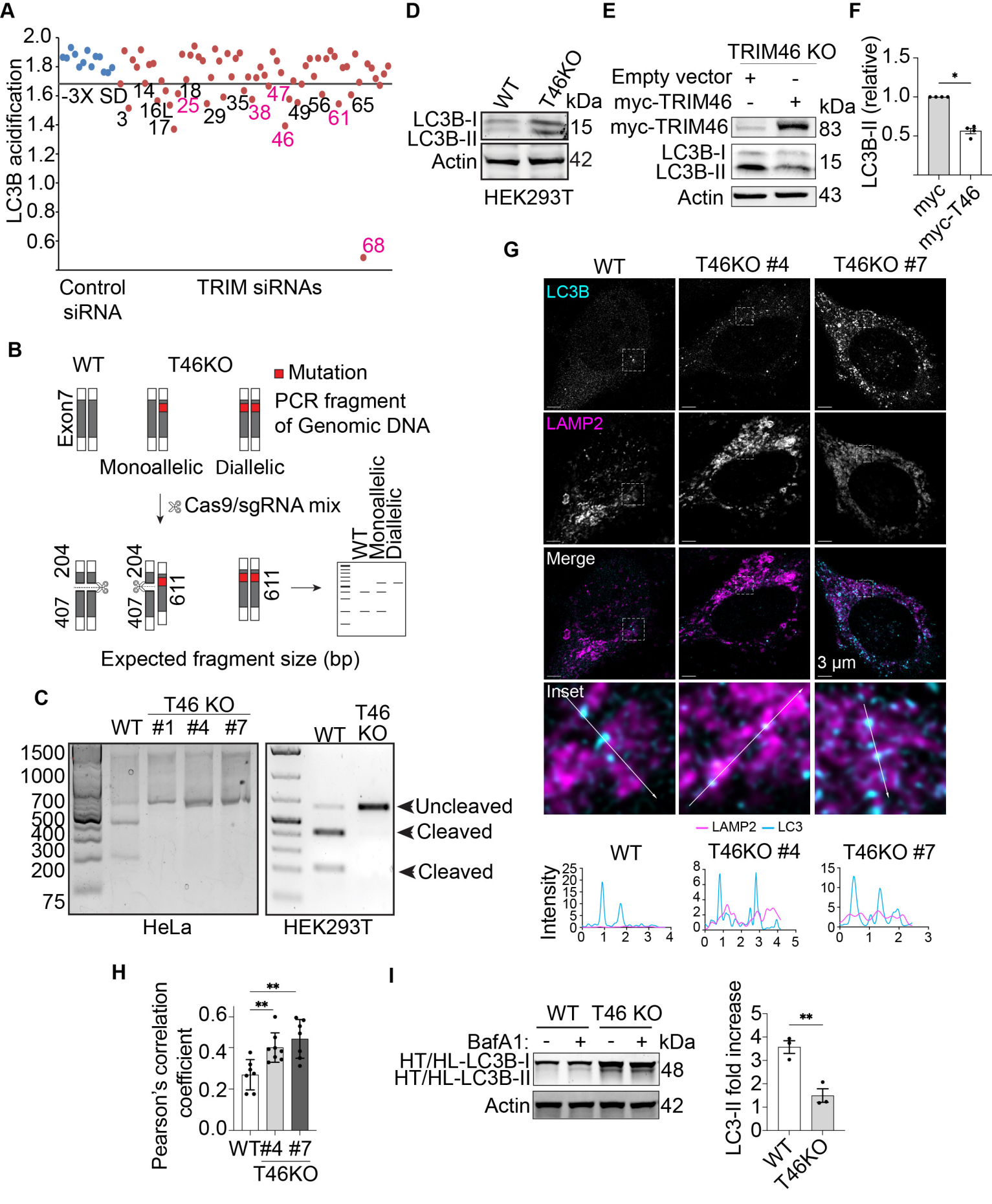
A
LC3B acidification
-3X SD
Control siRNA
TRIM siRNAs
B
WT
T46KO
Mutation
PCR fragment of Genomic DNA
Exon7
Monoallelic
Diallelic
Cas9/sgRNA mix
Expected fragment size (bp)
C
T46 KO
WT #1 #4 #7
HeLa
HEK293T
Uncleaved
Cleaved
D
WT
T46KO
kDa
LC3B-I
LC3B-II
Actin
HEK293T
E
TRIM46 KO
Empty vector
myc-TRIM46
F
LC3B-II (relative)
myc
myc-T46
G
WT
T46KO #4
T46KO #7
LC3B
LAMP2
Merge
3 µm
Inset
LAMP2
LC3
Intensity
H
Pearson's correlation coefficient
WT#4 #7
T46KO
I
WT T46 KO
BafA1:
HT/HL-LC3B-I
HT/HL-LC3B-II
LC3-II fold increase

**Figure S1**

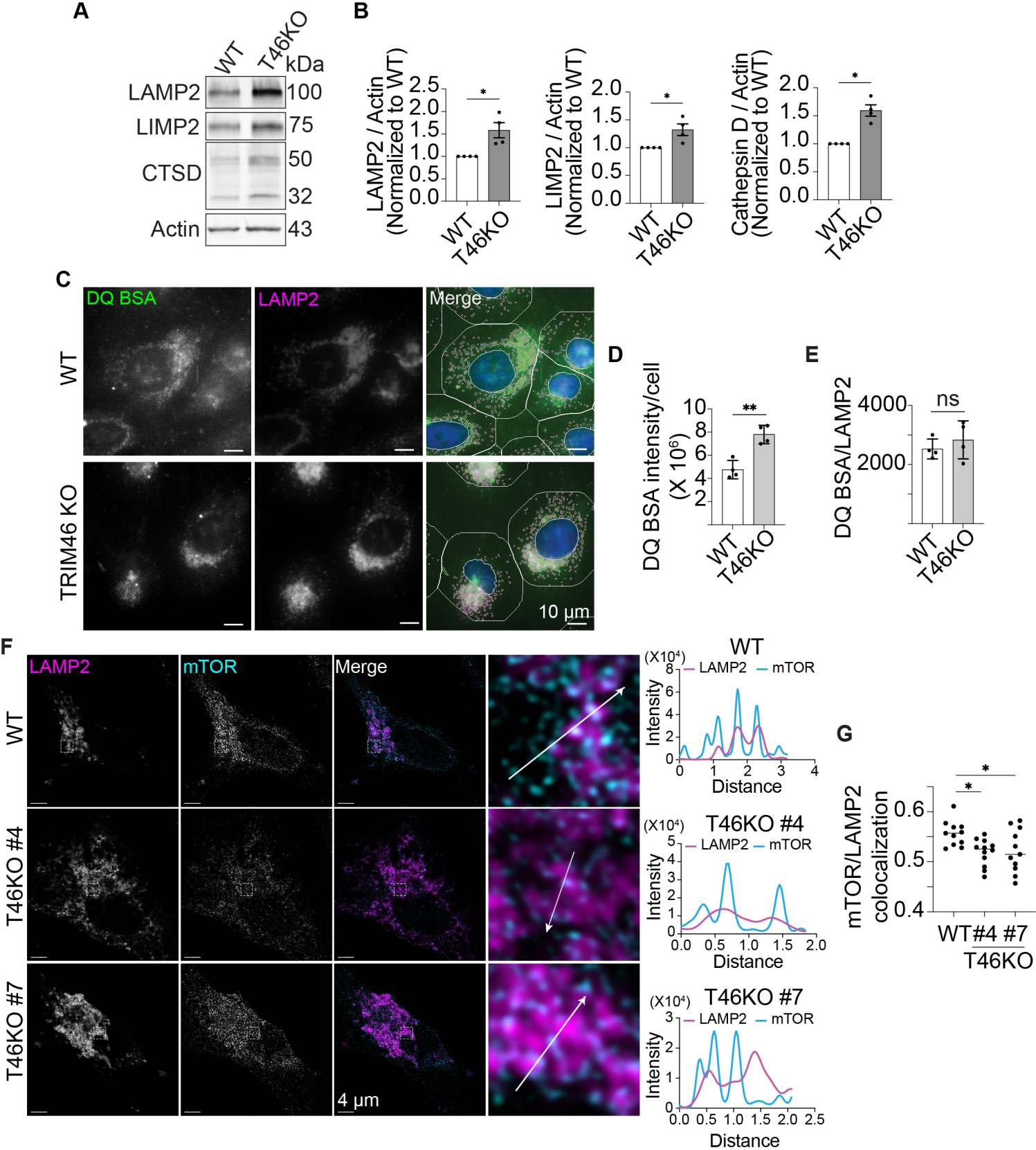
A
WT
T46KO
kDa
LAMP2
100
LIMP2
75
CTSD
50
32
Actin
43
B
LAMP2 / Actin (Normalized to WT)
LIMP2 / Actin (Normalized to WT)
Cathepsin D / Actin (Normalized to WT)
WT
T46KO
C
DQ BSA
LAMP2
Merge
WT
TRIM46 KO
10 µm
D
DQ BSA intensity/cell (X 10^6)
E
DQ BSA/LAMP2
ns
F
LAMP2
mTOR
Merge
T46KO #4
T46KO #7
4 µm
(X10^4)
Intensity
Distance
G
mTOR/LAMP2 colocalization
WT
#4
#7
T46KO

**Figure S2**

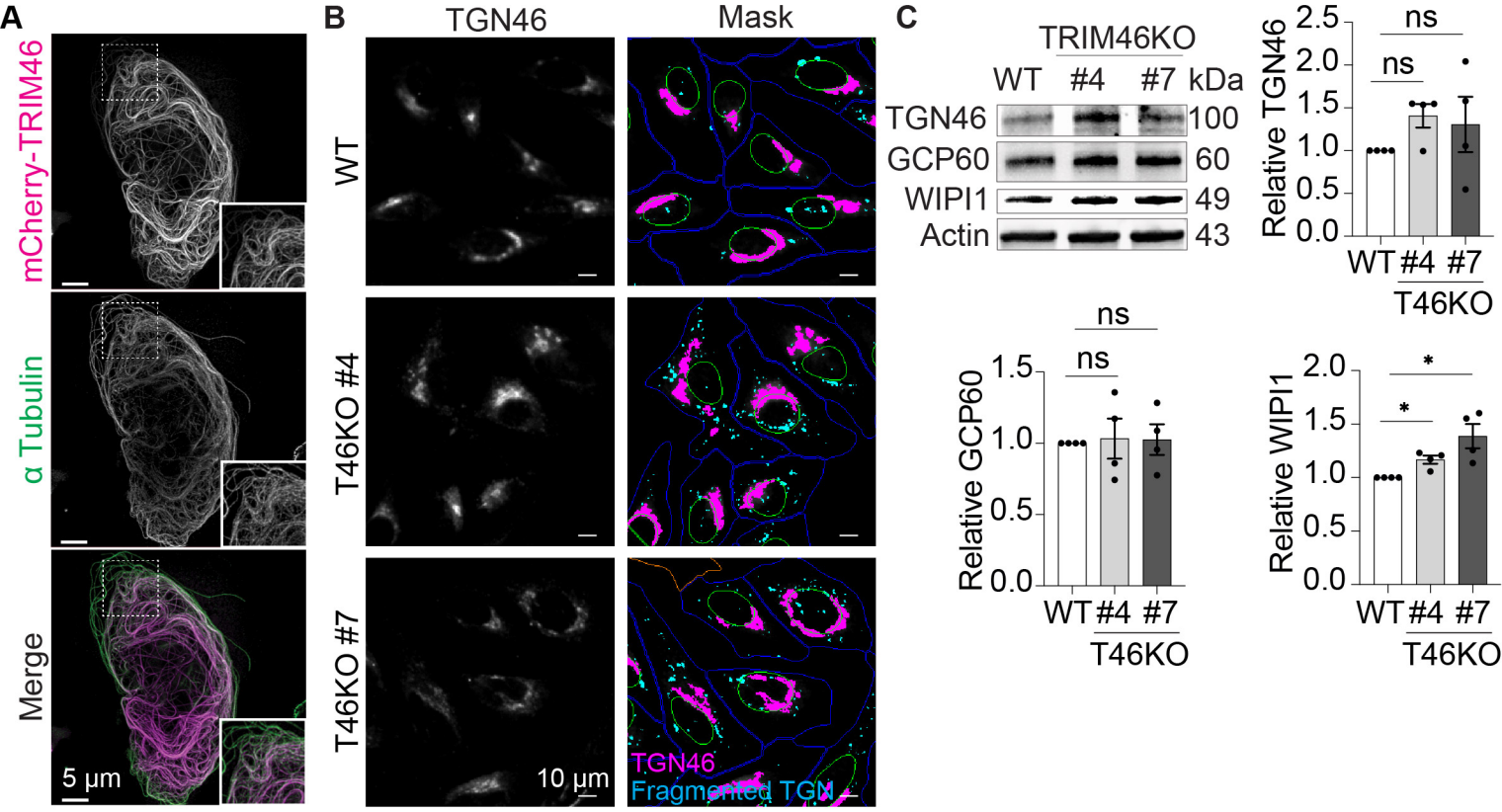
A
mCherry-TRIM46
α Tubulin
Merge
5 µm
B
TGN46
Mask
WT
T46KO #4
T46KO #7
10 µm
TGN46
Fragmented TGN
C
TRIM46KO
WT #4 #7 kDa
TGN46 100
GCP60 60
WIPI1 49
Actin 43
Relative TGN46
ns
ns
WT #4 #7
T46KO
Relative GCP60
ns
ns
WT #4 #7
T46KO
Relative WIPI1
*
*
WT #4 #7
T46KO

**Figure S3**

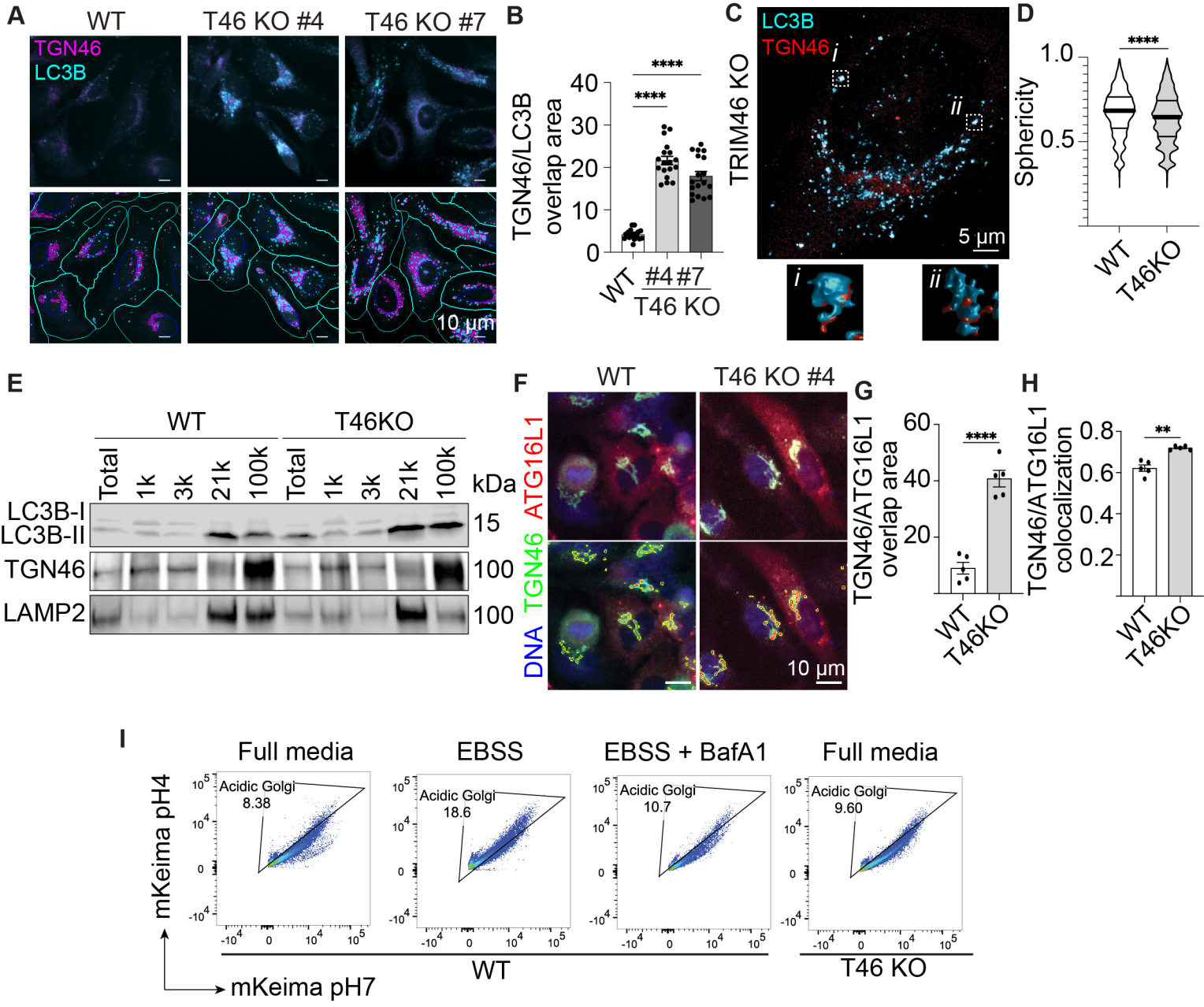
A
WT
T46 KO #4
T46 KO #7
TGN46
LC3B
10 µm
B
TGN46/LC3B overlap area
****
****
WT
#4 #7
T46 KO
C
LC3B
TGN46
TRIM46 KO
i
ii
5 µm
D
Sphericity
****
WT
T46KO
E
WT
T46KO
Total
1k
3k
21k
100k
kDa
LC3B-I
LC3B-II
TGN46
LAMP2
15
100
100
F
WT
T46 KO #4
ATG16L1
TGN46
DNA
10 µm
G
TGN46/ATG16L1 overlap area
****
WT
T46KO
H
TGN46/ATG16L1 colocalization
**
WT
T46KO
I
Full media
EBSS
EBSS + BafA1
Full media
Acidic Golgi
8.38
Acidic Golgi
18.6
Acidic Golgi
10.7
Acidic Golgi
9.60
mKeima pH4
mKeima pH7
WT
T46 KO

**Figure S4**

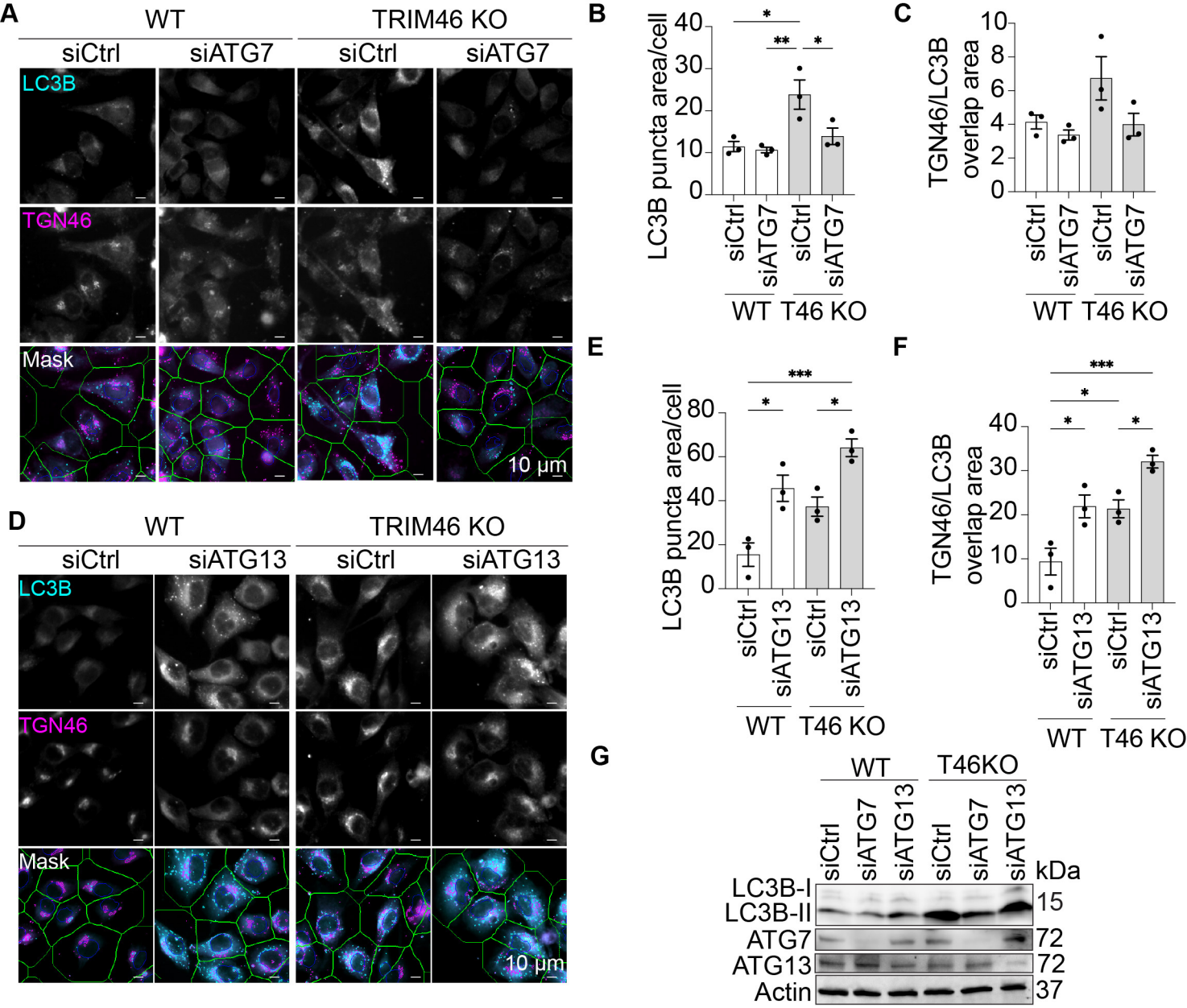
A
WT
TRIM46 KO
siCtrl
siATG7
siCtrl
siATG7
LC3B
TGN46
Mask
10 μm
B
LC3B puncta area/cell
C
TGN46/LC3B overlap area
WT
T46 KO
D
WT
TRIM46 KO
siCtrl
siATG13
siCtrl
siATG13
LC3B
TGN46
Mask
10 μm
E
LC3B puncta area/cell
F
TGN46/LC3B overlap area
G
WT
T46KO
siCtrl
siATG7
siATG13
siCtrl
siATG7
siATG13
kDa
LC3B-I
LC3B-II
ATG7
ATG13
Actin
15
72
72
37

**Figure S5**

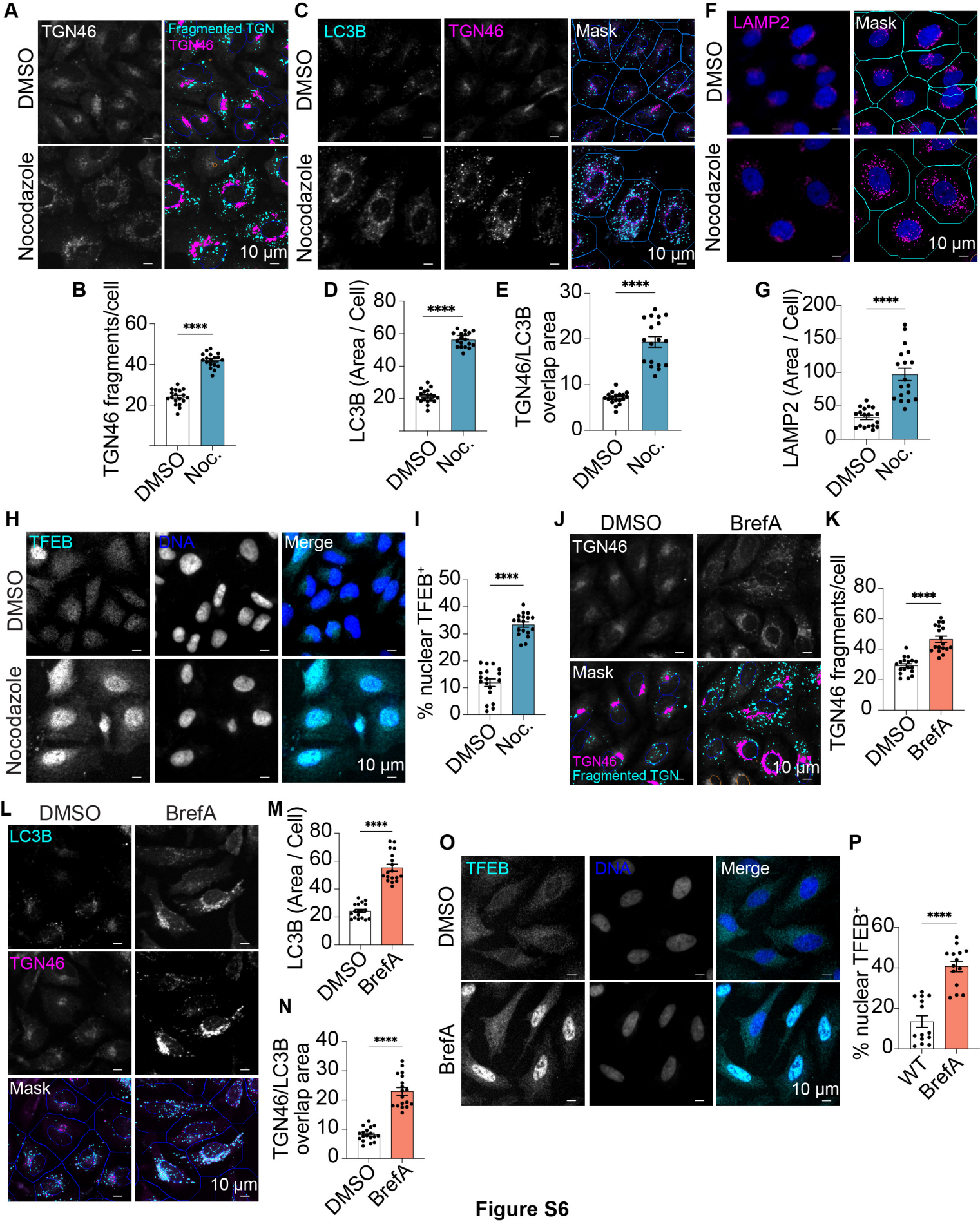
A
TGN46
Fragmented TGN
TGN46
DMSO
Nocodazole
10 µm
B
TGN46 fragments/cell
****
DMSO
Noc.
C
LC3B
TGN46
Mask
DMSO
Nocodazole
10 µm
D
LC3B (Area / Cell)
****
DMSO
Noc.
E
TGN46/LC3B overlap area
****
DMSO
Noc.
F
LAMP2
Mask
DMSO
Nocodazole
10 µm
G
LAMP2 (Area / Cell)
****
DMSO
Noc.
H
TFEB
DNA
Merge
DMSO
Nocodazole
10 µm
I
% nuclear TFEB+
****
DMSO
Noc.
J
DMSO
BrefA
TGN46
Mask
TGN46
Fragmented TGN
10 µm
K
TGN46 fragments/cell
****
DMSO
BrefA
L
DMSO
BrefA
LC3B
TGN46
Mask
10 µm
M
LC3B (Area / Cell)
****
DMSO
BrefA
N
TGN46/LC3B overlap area
****
DMSO
BrefA
O
TFEB
DNA
Merge
DMSO
BrefA
10 µm
P
% nuclear TFEB+
****
WT
BrefA

**Figure S6**